REPORT DOCUMENTATION PAGE

Form Approved
OMB NO. 0704-0188

1. AGENCY USE ONLY (Leave Blank)	2. REPORT DATE 10/29/04	3. REPORT TYPE AND DATES COVERED **Final Report (1/26/01 – 8/31/04)**

4. TITLE AND SUBTITLE
Advanced Electromagnetic Modeling

5. FUNDING NUMBERS
MDA972-01-1-0022

6. AUTHOR(S)
Stephen D. Gedney

7. PERFORMING ORGANIZATION NAME(S) AND ADDRESS(ES)
University of Kentucky
Department of Electrical and Computer Engineering
453 Anderson Hall, Lexington, KY 40506-0046

8. PERFORMING ORGANIZATION REPORT NUMBER
Tech Report EMG-04-001

9. SPONSORING / MONITORING AGENCY NAME(S) AND ADDRESS(ES)

Defense Advanced Research Projects Agency
Design Sciences Office
3701 North Fairfax Drive
Arlington, VA 22203-1714

10. SPONSORING / MONITORING AGENCY REPORT NUMBER

11. SUPPLEMENTARY NOTES
The views, opinions and/or findings contained in this report are those of the author(s) and should not be construed as an official position of DARPA, policy or decision, unless so designated by other documentation.

12 a. DISTRIBUTION / AVAILABILITY STATEMENT

Approved for public release; distribution unlimited.

12 b. DISTRIBUTION CODE

13. ABSTRACT (Maximum 200 words)

This report presents a fast, high-order hybrid volume/surface integral equation formulation developed under the DARPA VET program for the electromagnetic scattering by composite material targets. The solution is based on a high-order method of moment discretization with quadrature point collocation scheme, shown to be equivalent to the Locally Corrected Nyström formulation. The general solution procedure has been incorporated into the University of Kentucky *Mat-Scat* software. *Mat-Scat* also supports fast iterative solvers, including the Quadrature-Sampled Pre-Corrected FFT and the Fast Multipole Method. Also discussed is a high-order mesh processing software, *MeshTool*, used to generate high-order mesh descriptions of complex objects for simulation via *Mat-Scat*.

14. SUBJECT TERMS
Electromagnetic scattering
Radar Cross Section
high-order solution method, fast solution methods
Locally Corrected Nyström Method

15. NUMBER OF PAGES
44

16. PRICE CODE

17. SECURITY CLASSIFICATION OR REPORT	18. SECURITY CLASSIFICATION ON THIS PAGE	19. SECURITY CLASSIFICATION OF ABSTRACT	20. LIMITATION OF ABSTRACT
UNCLASSIFIED	**UNCLASSIFIED**	**UNCLASSIFIED**	**UL**

Table of Contents

1. Program Overview

This research program has focused on the development of novel numerical techniques for the solution of electromagnetic scattering problems that are accurate, fast, and robust. The specific advancements of this program have been:

i) The derivation of a high-order method of moment formulation with a quadrature point collocation scheme that is equivalent to a locally-corrected Nyström (LCN) method.

ii) The development of mixed-order basis functions for general LCN formulations.

iii) The demonstration of a high-order LCN formulation for the electromagnetic scattering by inhomogeneous material regions.

iv) The development of a hybrid volume/surface integral equation formulation for the electromagnetic scattering by composite material objects.

v) The development of computer software (*Mat-Scat*) for the simulation of the electromagnetic scattering by composite material objects based on a high-order LCN formulation.

vi) The application of fast iterative solvers within *Mat-Scat*, and the development of the Quadrature-Sampled Pre-Corrected FFT (QS-PCFFT) formulation.

vii) The validation of the high-order solution techniques for a number of scattering problems.

2. Accomplishments

Through the course of this program, the following milestones have been accomplished.

2.A High-order method of moment solution with Point-Based Discretization

We have developed a new method of moment methodology based on high-order basis functions and a quadrature point collocation scheme [1, 2]. By applying an efficient far-field transformation, the degrees of freedom can be mapped from the basis function to the quadrature points leading to a form that is identical to the Locally Corrected Nyström (LCN) method [3]. The high-order method leads to exponential convergence for smooth scatterers [2]. Exponential convergence has also been demonstrated for geometries with edge singularities through the use of singular basis and specialized quadrature rules [2, 4]. For arbitrary geometries, we have also demonstrated that the use of divergence-conforming mixed-order basis functions can significantly improve the accuracy of the method and greatly improve the condition number of the impedance matrix [5].

2.B High-order solution for the scattering by inhomogeneous material volumes.

A method of moment formulation with quadrature point sampling for the scattering by inhomogeneous material volumes has been developed and validated. The method has been shown to yield exponential convergence for canonical and non-canonical scatterers [6-9]. This is the first known integral-equation based electromagnetic scattering solution with a high-order representation of a material inhomogeneity.

2.C Hybrid Surface/Volume integral equation formulation

A novel integral equation method has been derived for a general hybrid surface/volume formulation. The integral equation formulation allows for the combination of arbitrary material surfaces, including conducting as well as penetrable materials, and inhomogeneous volumes. A computer program (identified as: *Mat-Scat*) implementing this technique using the proposed high-order method of moment formulation has been developed. The code has been fully validated for curvilinear quadrilateral and hexahedral cells with orthogonal mixed-order divergence conforming basis functions and quadrature point collocation.

2.D Fast Solution Methods

2.D.1 Quadrature Sampled Pre-Corrected FFT (QS-PCFFT)

A novel solution algorithm referred to as the "Quadrature Sampled Pre-Corrected FFT" (QS-PCFFT) algorithm has been developed [4, 9]. This method is in the same class of methods as the PC-FFT [10] and the Adaptive Integral Method (AIM) [11]. The principal difference is that moments are never explicitly computed. Rather, the projection from the general discretization to the uniform grid is performed efficiently and to high order using Gaussian quadrature. The method naturally preserves the high-order convergence of the method of moment solution, even for singular basis functions [4]. The method scales as $O(N\log N)$ for the scattering by material volumes or planar structures and $O(N^{3/2}\log N)$ for surface scattering. The QS-PCFFT algorithm has been implemented within *Mat-Scat*.

2.D.2 Multilevel Fast Multipole Method

A fast iterative solver based on the multi-level fast multipole solution [12-15] has also been implemented within *Mat-Scat*. The multi-level scheme is based on the algorithm proposed by Gyuer and Stalzer [16], and the fast spherical filtering scheme of Jakob-Chien and Alpert [17] was implemented to accelerate the disaggregation step of the MLFMM algorithm.

2.E High-Order Mesh Generation

The University of Kentucky scattering code *Mat-Scat* is capable of handling surface and volume elements of arbitrary order. The majority of commercially available mesh generation schemes are limited typically limited to quadratic or cubic elements. For the modeling of more complex geometries, an automated tool must be available for generating high-order meshes. Thus, we have developed a high-order mesh generation tool. The initial surface description and low-order mesh is first entered into a commercial tool such as SDRC Ideas™. The UK mesh tool can convert the coarse low order mesh into a high-order mesh with elements of arbitrary order. Other post-processing tools, such as extrusion to an arbitrary surface (e.g., for the modeling of thin material coatings) and mesh quality checking have also been included. A

graphical user interface (GUI) has been developed for the tool using JAVA. This makes the toll convenient to use and platform platform independent.

3. Subcontractors/Team Members

There are no subcontractors on this awarded.

Faculty Members of the University Kentucky VET Program:
Prof. Stephen D. Gedney
Prof. Cai-Cheng Lu

Post-Doctoral Research Associates funded under this program:
Dr. Jens Hannemann, Post-Doctoral Research Associate.
Dr. Regina Hannemann, Post-Doctoral Research Associate.

Graduate Students Funded under this Program:
Dr. Aiming Zhu

Undergraduate students funded under this program:
Ryan Chilton, Undergraduate Research Assistant

The University of Kentucky was also teamed with HRL Laboratories, LLC, and FMAHC.

4. Summary of Results

4.A High-order method of moment solution with Point-Based Discretization

4.A.1 Formulation

Consider the integral equation used to solve for a surface current density $J(\vec{r}')$:

$$\phi^{inc}(\vec{r}) = \int_S K(\vec{r},\vec{r}')J(\vec{r}')ds' \tag{1}$$

where S is a smooth surface, $\phi^{inc}(\vec{r})$ is the known forcing function evaluated at position $\vec{r}$ on S, $K(\vec{r},\vec{r}')$ is the kernel. S is discretized into N_p curvilinear patches that represent the surface contour to high-order. The surface current $J(\vec{r}')$ is approximated over each patch by a basis function expansion:

$$J(\vec{r}) \approx \sum_{k=1}^{N_k} b_{k_p} F_k(\vec{r}) \tag{2}$$

where, b_{k_p} are constant coefficients and $F_k(\vec{r}')$ represent a set of smooth basis functions distributed over the p^{th} patch that is complete to order N_k. A set of smooth test functions $T_l(\vec{r})$ with support over each patch and complete to order N_k is introduced. The inner product of (1) with each of the test functions is then performed, leading to:

$$\int_S T_l(\vec{r})\phi^{inc}(\vec{r})ds = \int_S T_l(\vec{r})\left[\sum_{p=1}^{N_p}\sum_{k=1}^{N_k} b_{k_p}\int_{S_p} K(\vec{r},\vec{r}')F_k(\vec{r}')ds'\right]ds\,. \tag{3}$$

On the m-th patch, the outer integral of (3) is approximated using a N_k-point quadrature rule that integrates exactly functions to at least order N_k:

$$\sum_{q=1}^{N_k} T_l(\vec{r}_{q_m})\phi^{inc}(\vec{r}_{q_m}) = \sum_{q=1}^{N_k} T_l(\vec{r}_{q_m})\left[\sum_{p=1}^{N_p}\sum_{k=1}^{N_k} b_{k_p}\int_{S_p} K(\vec{r}_{q_m},\vec{r}')F_k(\vec{r}')ds'\right] \tag{4}$$

After applying a simple linear transformation (see equations (5)-(7) in [1]), (4) is reduced to:

$$\phi^{inc}(\vec{r}_{q_m}) = \sum_{p=1}^{N_p}\sum_{k=1}^{N_k} b_{k_p}\int_S K(\vec{r}_{q_m},\vec{r}')F_k(\vec{r}')ds' \tag{5}$$

where $\vec{r}_{q_m}$ is a quadrature abscissa point on the m^{th} patch. **The discrete form in (5) appears to be a method of moment formulation with a quadrature point collocation scheme. However, it is equivalent to a method of moment procedure employing test functions up to order N_k with the outer integral evaluated by a fixed-point quadrature rule.**

In the regions where the patches are sufficiently far from the observation point, the kernel is smooth and the convolutional integral in (5) can also be approximated to high-order by a fixed-point quadrature rule. Again, assuming an N_k-point rule that integrates smooth functions

exactly to at least order N_k, the contribution to the right-hand side of (5) from patches that are sufficiently far from $\vec{r}_{q_m}$ can be expressed as:

$$\sum_{p\in far}\sum_{k=1}^{N_k} b_{k_p}\left[\sum_{q=1}^{N_k}\omega_{q_p}K\left(\vec{r}_{q_m},\vec{r}_{q_p}\right)F_k\left(\vec{r}_{q_p}\right)\right] \tag{6}$$

where $\vec{r}_{q_p}$ are the abscissa points and ω_{q_p} are the weights of the quadrature rule. In operator form, (6) can be expressed as:

$$\left(\left[L_p\right]\bar{k}_{q_m}\right)^T\bar{b} = \bar{k}_{q_m}{}^T\left[L_p\right]^T\bar{b}, \tag{7}$$

where the matrix $[L_p]$ is matrix local to patch p with entries $[L_p]_{k,j} = F_k(\vec{r}_{j_p})$, the vector $\bar{k}_{q_m}$ is the kernel $K\left(\vec{r}_{q_m},\vec{r}_{q_p}\right)$ sampled at the quadrature points $\vec{r}_{j_p}$, and $\bar{b}$ is the vector of coefficients weighting the basis functions. It is then recognized that

$$\bar{j} = \left[L_p\right]^T\bar{b}, \tag{8}$$

where $\bar{j}$ are the currents evaluated at the discrete quadrature points. Thus, (8) implies a transformation of unknowns from the current basis to the quadrature points. This transformation is then carried into the near field region. In this region, the convolutional integral in (5) must be performed via adaptive quadrature to desired precision. In operator form, this is expressed as:

$$\bar{\kappa}_{q_m}^T\bar{b} \tag{9}$$

where the k-th element of vector $\bar{\kappa}_{q_m}$ is $= \int_{S_p} K\left(\vec{r}_{q_m},\vec{r}'\right)F_k\left(\vec{r}'\right)ds'$, which is evaluated to desired precision using adaptive quadrature. Next, applying the transformation of variables in (8), $\bar{b} = [L_p^{-1}]^T\bar{J}$ and (9) is rewritten as:

$$\bar{\kappa}_{q_m}^T\left[L_p^T\right]^{-1}\bar{j} = \left\{\left[L_p\right]^{-1}\bar{\kappa}_{q_m}\right\}^T\bar{j} \tag{10}$$

In summary, the contribution to the q_m-th row of the impedance matrix derived via the method of moment procedure for far interaction can be expressed from (7) and (8) as:

$$Z_{q_m}^{far} = \left(\bar{k}_{q_m}\right)^T \tag{11}$$

and for near interaction from (10) as:

$$Z_{q_m}^{near} = \left\{\left[L_p\right]^{-1}\bar{\kappa}_{q_m}\right\}^T. \tag{12}$$

It is observed that both (11) and (12) are identical to that derived via the Locally Corrected Nyström (LCN) method [2, 3]. **Consequently, the proposed high-order method of moment (HO-MoM) procedure is equivalent to a LCN formulation. However, it is derived using a more classical paradigm understood by most practitioners.**

4.A.2 Mixed-Order Basis Functions

When applying the high-order method of moment (or LCN) procedure, it is assumed that the surfaces or volumes of the model are discretized using general curvilinear cells that model the surfaces to sufficient accuracy. The current density is then expanded over each cell with a set of local vector basis functions. As an illustration, we can assume general curvilinear quadrilateral surface cells. A basis function expansion for the current can be represented in the form:

$$\vec{J}_1\left(u^1,u^2\right)=b_1^{j_1,k_1}\vec{a}_1P_{j_1}\left(u^1\right)P_{k_1}\left(u^2\right)/\sqrt{g}\quad\left(j_1=0..M_1^1;k_1=0..M_1^2\right),\tag{13}$$

$$\vec{J}_2\left(u^1,u^2\right)=b_2^{j_2,k_2}\vec{a}_2P_{j_2}\left(u^1\right)P_{k_2}\left(u^2\right)/\sqrt{g}\quad\left(j_2=0..M_2^1;k_2=0..M_2^2\right),\tag{14}$$

where, following the notation of Stratton [18], (u^1,u^2) are the local curvilinear coordinates of the quadrilateral cell, $\vec{a}_i$ are the local unitary vectors, $\sqrt{g}$ is the Jacobian, $P_j(u)$ are j^{th}-order Legendre polynomials, and $b_i^{j,k}$ are unknown constant coefficients. The order of the basis functions are specified by M_s^t. Classically, the LCN method has been proposed using a basis order that is complete to polynomial order p [2, 3]. In this situation, $M_1^1=M_1^2=M_2^1=M_2^2=p$. This is referred to here as a polynomial-complete basis function set. Alternatively, a mixed-order basis function can be posed that is divergence conforming. That is, the divergence of the current density, which is directly proportional to the charge density, is complete to a polynomial order. This is accomplished if the current density is a mixed-order. A p-th order mixed-order basis function set is then proposed with $M_1^1=M_2^2=p+1$ and $M_1^2=M_2^1=p$.

The electric surface charge density within the boundaries of a surface cell is:

$$\begin{aligned}\rho_e&=-\frac{1}{j\omega}\nabla_t\cdot\vec{J}=-\frac{1}{j\omega}\sum_{i=1}^{2}\frac{1}{\sqrt{g}}\frac{\partial}{\partial u^i}\left(\sqrt{g}\vec{a}^i\cdot\vec{J}_t\right)\\&=-\frac{1}{j\omega}\left[b_1^{j_1,k_1}\frac{\partial P_{j_1}\left(u^1\right)}{\partial u^1}P_{k_1}\left(u^2\right)+b_2^{j_2,k_2}P_{j_2}\left(u^1\right)\frac{\partial P_{k_2}\left(u^2\right)}{\partial u^2}\right]/\sqrt{g}\end{aligned}\tag{15}$$

where the range of j and k is governed by the type of basis function used. If a polynomial complete basis is used, the charge density is represented by an incomplete polynomial expansion. In fact, the highest-order basis function pairs ($j_{1,2}=k_{1,2}=p$, $i=1,2$) will produce surface charge densities that are of mixed order. On the other hand, the mixed-order basis leads to a surface charge density that is polynomial complete to order p.

It was shown in [19] by Çalışkan and Peterson as well as Gedney [5] that the polynomial-complete basis can lead to spurious solutions for geometries with edge singularities and that this can be remedied through the use of the mixed-order basis. This is somewhat intuitive for the following reason. If one observes the charge density at the singular edge, one expects the charge density to exhibit the same leading-order singularity as the current flowing transverse to the edge and as the normal derivative of the current flowing normal to the edge. This can be well

approximated by the mixed-order basis. For the polynomial complete basis this is approximated by the lower-order terms, but there are additional spurious charges from the highest-order basis that will exist. For smooth scatterers, this does not occur and consequently either basis function can be used successfully. However, since the charge density is over-specified by the polynomial-complete basis, a poorly conditioned system results for the EFIE operator.

When employing the mixed-order basis functions presented, an appropriate testing scheme must be implemented within the context of the LCN method. There are two choices. The first is that one can employ a single quadrature rule for a cell and then use a least square solution for the over or under-determined system to calculate the local corrections. The other alternative is to employ a pair of mixed-order quadrature rules – one for each test vector – and solve a square matrix for the local corrections. We have implemented the latter option.

Consider the mixed-order basis in which the charge density is polynomial complete to order p. Two test vectors $\vec{t}_1$ and $\vec{t}_2$ are introduced. Each of the two test vectors are associated with a quadrature rule that is consistent with the order of the basis functions $\vec{J}_1$ and $\vec{J}_2$. That is, given $\vec{J}_1$ to be of order $(p+1)\times p$, a $(p+1)\times p$ point quadrature rule is defined for the quadrilateral patch (this is done here as a product of one-dimensional Gauss-quadrature rules). The inner dot product of the integral operator with $\vec{t}_1$ is then performed at each discrete quadrature abscissa point. Similarly, the inner dot product of the integral operator with $\vec{t}_2$ is performed at the abscissa points of a $p\times(p+1)$ point quadrature rule. In this manner, a square linear system of equations results for the local corrections following the procedure outlined in [2, 3].

4.B High-Order Solution of the Volume Field Integral Equation

An inhomogeneous and isotropic dielectric object with relative permittivity $\varepsilon_r(\vec{r})$ contained within a volume V and situated in a homogeneous free space is illuminated by an incident electromagnetic field $\vec{E}^{inc}$ with an $e^{j\omega t}$ time dependence. The scattered field resulting from the impinging wave can be computed through the use of equivalent volume currents that are distributed within V and that satisfy the electric field integral equation (EFIE) [20-22]:

$$\vec{E}^i(\vec{r}) = \frac{\vec{J}(\vec{r})}{j\omega\varepsilon_o(\varepsilon_r(\vec{r})-1)} + jk_o\eta_o \iiint_V \bar{\bar{G}}(\vec{r},\vec{r}')\cdot\vec{J}(\vec{r}')dv' \tag{16}$$

where $\vec{E}^i$ is the incident electric field in the absence of the dielectric cylinder, k_o is the free space wave number, η_o is the free space wave impedance, $\bar{\bar{G}}$ is the dyadic Green's function:

$$\bar{\bar{G}}(\vec{r},\vec{r}') = \left(\bar{\bar{I}} + \frac{1}{k_o^2}\nabla\nabla\right) g_o(\vec{r},\vec{r}') \tag{17}$$

$g_o(\vec{r},\vec{r}') = e^{-jk_o|\vec{r}-\vec{r}'|}/4\pi|\vec{r}-\vec{r}'|$ is the free-space Green's function, and $\vec{J}(\vec{r})$ is the equivalent polarization current density distributed over V which is defined as:

$$\vec{J}(\vec{r}) = j\omega\varepsilon_o \vec{E}^{tot}(\vec{r})(\varepsilon_r(\vec{r})-1). \tag{18}$$

where $\vec{E}^{tot}$ is the total electric field in V.

The solution to the EFIE in (16) will be obtained via the high-order method of moment scheme proposed in [2]. To this end, V is discretized with volumetric curvilinear cells that represent the surface defining V to high order. Within each cell, the current is expanded using a set of smooth vector basis functions that are complete to order p. A p-point Gauss-quadrature rule of order $2p$-1 and with abscissas and weights $(\vec{r}_m, \omega_m)$ is introduced over each volume cell. At each quadrature point three-independent test vectors are introduced $\vec{t}_m$. A point-matched formulation is obtained by sampling (16) at the quadrature points, leading to:

$$\vec{t}_m \cdot \vec{E}^i(\vec{r}) = \frac{\vec{t}_m \cdot \vec{J}(\vec{r}_m)}{j\omega\varepsilon_o(\hat{\varepsilon}_r(\vec{r}_m)-1)} + j\eta_o k_o \vec{t}_m \cdot \iiint_V \left[\bar{\bar{G}}(\vec{r}_m,\vec{r}')\cdot\vec{J}(\vec{r}')\right]dv' \tag{19}$$

It is shown in [2] that the formulation in (19) is equivalent to that employing p^{th} order test functions and a fixed point quadrature rule. It is also shown in [2] to be equivalent to a locally corrected Nyström (LCN) formulation [3].

The volume V defined by the dielectric scatterer is assumed to be discretized by curvilinear cells. The cells are currently assumed to be curvilinear hexahedron. Each cell is uniquely described by a local curvilinear coordinate system. The current within each hexahedron is expanded via a set of vector basis functions weighted by constant coefficients b_n as:

$$\vec{J}(\vec{r}) \approx \sum_{n=1}^{N} b_n \vec{j}_n(\vec{r}), \tag{20}$$

where the $\vec{j}_n$ are the mixed-order basis defined in (13) modified for a three-dimensional hexahedral cell. The test vectors are also chosen as the reciprocal unitary vectors so that $\vec{t}_m \cdot \vec{j}_n = 0$ if $m \neq n$.

A quadrature rule is also defined for each cell. For hexahedron, the rule is conveniently defined via a product rule of one-dimensional Gauss-Legendre quadratures. Note that a mixed-order quadrature rule is used for each basis function, leading to a square linear system of equations.

To validate this scheme, consider the scattering by a spherical shell with a continuous radial inhomogeneity. The relative permittivity of the sphere is defined as:

$$\varepsilon_r(r) = \begin{cases} 2.0 + \dfrac{(r-a)^2}{(b-a)^2}7.0, & a < r < b \\ 1, & \text{elsewhere} \end{cases} \tag{21}$$

where a = 0.3 m, and b = 0.5 m. The relative permittivity thus varies from 2.0 at the inner radius to 9.0 at the outer radius with a quadratic profile. The shell was modeled with only a single layer

of curvilinear hexahedral cells (a total of 24 cells) that exactly represented the inner and outer surfaces. The continuous dielectric profile was then modeled exactly within the curvilinear cell through the diagonal term in (19). The volume current density and RCS were computed using the proposed high-order scheme. The bi-static RCS of the shell resulting from axially incident vertically and horizontally polarized waves is illustrated in Fig. 1 for two different basis orders and is compared against the exact solution. For a basis order of $3\times3\times3$, there is some apparent error in the RCS (about 1 dB on average). For a basis order of $4\times4\times4$, the predicted RCS is indistinguishable from the exact solution at the given resolution of the graph.

The mean relative error in the RCS as a function of unknowns for a single layer of 24 hexahedral cells and various orders is illustrated in Fig. 2. The error is computed relative to the known analytical solution. Superimposed in this graph is the mean absolute error in the total electric field, again referenced to the analytical solution. Note that the maximum electric field magnitude in the shell was about 3 V/m. Exponential convergence is realized by the high-order method.

The next case studied is a dielectric ogive shell. The geometry of this object is illustrated in Fig. 3. The shell has a uniform thickness of 0.05 m and is composed of a homogeneous dielectric with $\varepsilon_r = 2.56$. The ogive was discretized using a single layer of curvilinear hexahedron (as illustrated in Fig. 3). The mesh was generated using a commercial mesh generator and cubic elements were used. The bistatic RCS of the ogive in the $\theta = 90°$ plane is illustrated in Fig. 4 for two different discretizations and are compared to a reference solution that was finely discretized. For this simulation, the frequency was 299.796 MHz and the incident field was incident on the tip of the ogive ($\theta^{inc} = 90, \phi^{inc} = 0$). Both vertical and horizontal polarizations were simulated. The results are indistinguishable for the resolution presented. The mean relative error in the bistatic RCS versus the total number of unknowns is presented in Fig. 5. For this data, the error was computed relative to a finely discretized reference solution. For each curve, fixed discretizations were used - 24 cubic hexahedron and 56 cube hexahedron - and increasing order. For each data point, the basis order is provided on the graph (e.g., $4\times4\times2$). The first two orders are the transverse coordinates and the third is the radial. Overall, the solution exhibits exponential convergence - though there is a stutter in the convergence for the 56-cell discretization.

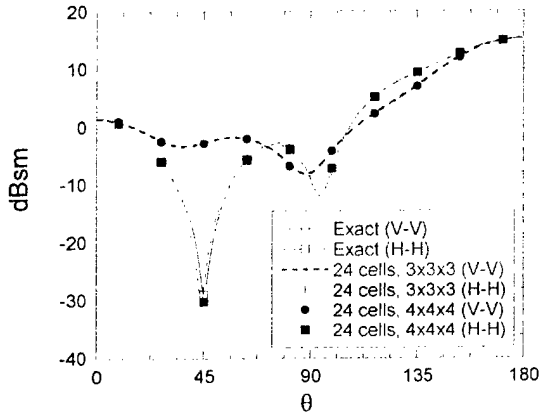

Fig. 1 Bistatic RCS of the spherical shell with radial inhomogeneous profile, for $\theta^{inc} = \phi^{inc} = 0°$ for V-V and H-H polarizations in the $\phi = 0°$ plane.

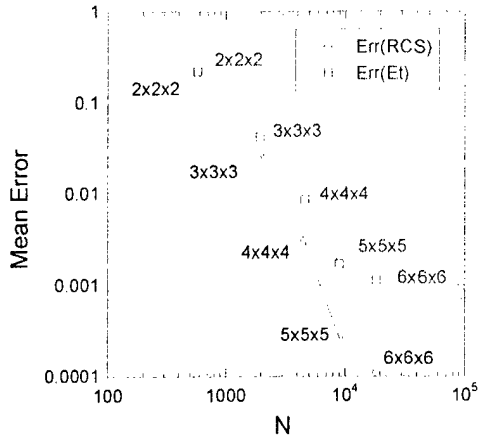

Fig. 2 Mean Error in the RCS (relative error) and the total electric field (absolute error) versus the total number of unknowns for a single layer of 24 hexahedral shells and increasing order for the inhomogeneous spherical shell.

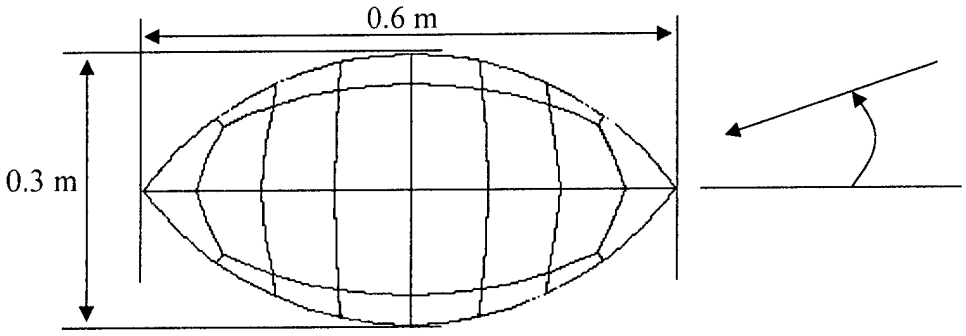

Fig. 3 Top view of the dielectric ogive shell (thickness = 0.05 m) and illustration of the 56-hexahedron mesh.

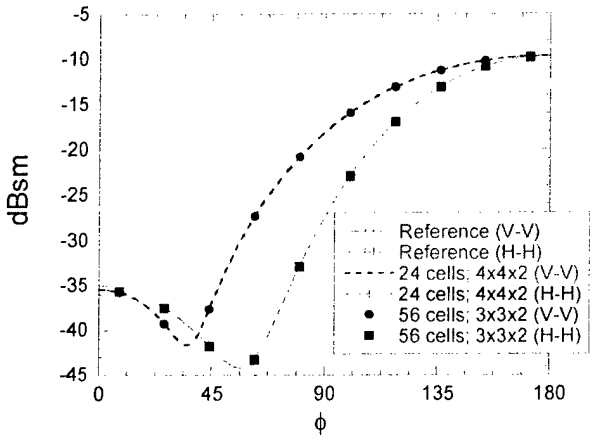

Fig. 4 Bistatic RCS of the dielectric ogive shell in the $\theta = 90°$ observation plane, for $\theta^{inc} = 90°$, $\phi^{inc} = 0°$ and a frequency of 299.796 MHz for V-V and H-H polarizations.

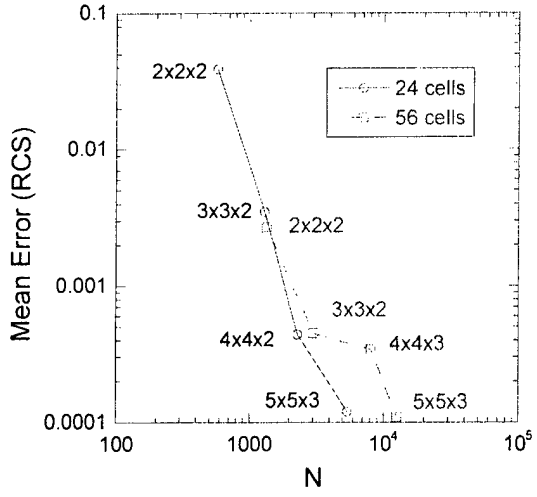

Fig. 5 Mean relative error in the RCS of the dielectric ogive shell versus the total number of unknowns for a single layer of hexahedral shells and increasing order.

4.C Hybrid Volume/Surface Field Integral Equation Solution

4.C.1 Formulation

Consider the electromagnetic interaction with an inhomogeneous material scatterer made of a composite of penetrable and conducting materials, as illustrated in Fig. 6. A radiating source with an $e^{j\omega t}$ time dependence can be placed either exterior or interior to the inhomogeneous object. Applying the equivalence principal, equivalent surface and volume sources are introduced that radiate the scattered field. From these sources, the integral equations will be posed that will allow for the unique solution of the equivalent sources.

Following Fig. 6, a surface separating volumes V_i and V_j is denoted as $S_{i,j}$. Let $S_{i,j}^+$ denote the surface just inside V_i, and $S_{i,j}^-$ the surface just inside V_j. Equivalent current densities are then placed on all surfaces separating each material volume. The surface current densities are located on either $S_{i,j}^+$ or $S_{i,j}^-$. Surface equivalent current densities on $S_{i,j}^+$ are posed as:

$$\vec{J}_{i,j}^{+} = \hat{n}_i \times \vec{H}\Big|_{S_{i,j}^+}, \quad \vec{M}_{i,j}^{+} = -\hat{n}_i \times \vec{E}\Big|_{S_{i,j}^+} \tag{22}$$

where $\hat{n}_i$ is the unit normal directed into V_i. Equivalent sources on surface $S_{i,j}^-$ are defined as:

$$\vec{J}_{i,j}^{-} = \hat{n}_j \times \vec{H}\Big|_{S_{i,j}^-}, \quad \vec{M}_{i,j}^{-} = -\hat{n}_j \times \vec{E}\Big|_{S_{i,j}^-} \tag{23}$$

where $\hat{n}_j$ is the normal directed into V_j. The upper and lower currents can be constrained by enforcing the continuity of the tangential fields on $S_{i,j}$, leading to the identity:

$$\vec{J}_{i,j}^{+} = -\vec{J}_{i,j}^{-} = \vec{J}_{i,j}, \quad \vec{M}_{i,j}^{+} = -\vec{M}_{i,j}^{-} = \vec{M}_{i,j}. \tag{24}$$

where it is recognized that $\hat{n}_j = -\hat{n}_i$. On the surface of a conductor, only the electric current density is supported. Consequently,

$$\vec{J}_{i,p} = \hat{n}_i \times \vec{H}\Big|_{S_{i,p}^+}. \tag{25}$$

Each material volume is assigned a *background* material profile $(\varepsilon_{ib}, \mu_{ib})$. This defines the volume equivalent currents within the material volume. Specifically, if $(\varepsilon_i, \mu_i) \neq (\varepsilon_{ib}, \mu_{ib})$

$$\begin{aligned} \vec{J}_{Vi} &= j\omega\varepsilon_o\varepsilon_{ib}\left(\frac{\varepsilon_{ir}}{\varepsilon_{ib}} - 1\right)\vec{E}, \\ \vec{M}_{Vi} &= j\omega\mu_o\mu_{ib}\left(\frac{\mu_{ir}}{\mu_{ib}} - 1\right)\vec{H} \end{aligned} \tag{26}$$

where $(\varepsilon_{ir}, \mu_{ir})$ is the relative permittivity and permeability of the physical material medium. Note that if $(\varepsilon_i, \mu_i) = (\varepsilon_{ib}, \mu_{ib})$, the volume current densities are identically zero. It is also noted that on any surface $S_{i,j}$, if $(\varepsilon_{ib}, \mu_{ib}) = (\varepsilon_{jb}, \mu_{jb})$, no surface current densities will be assigned to that surface.

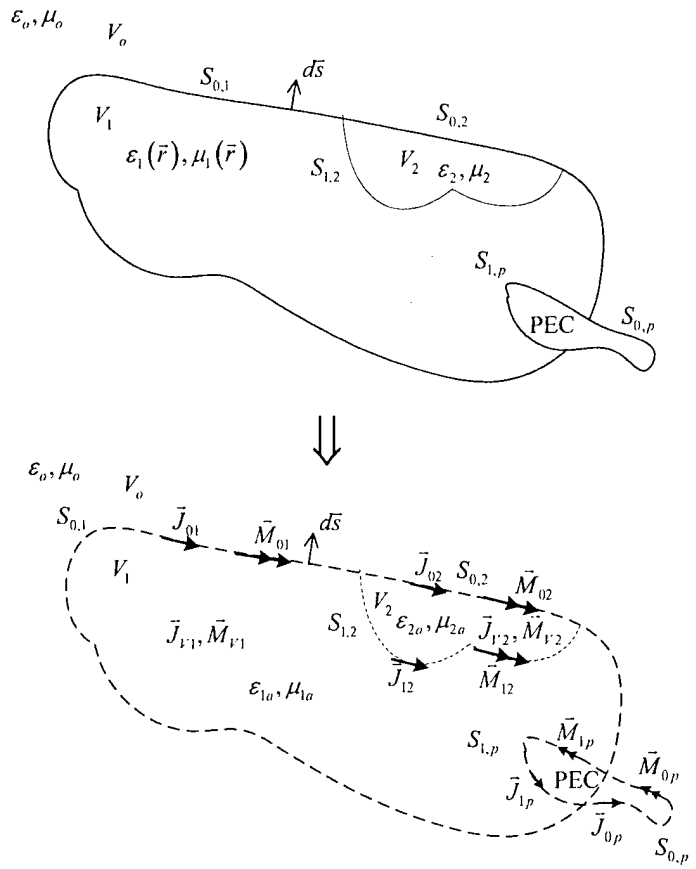

Fig. 6 Equivalent currents representing the scattered fields due to a plane wave impinging on an arbitrary inhomogeneous material scatterer.

Each equivalent current density is residing in an equivalent homogeneous material volume. For example, $\vec{J}^{+}_{i,j}$, $\vec{M}^{+}_{i,j}$, $\vec{J}_{Vi}$, $\vec{M}_{V_i}$ effectively radiate in a homogeneous space with material profile $(\varepsilon_{ih}, \mu_{ih})$. The equivalent currents are said to radiate a *scattered* field. The electric and magnetic scattered fields due to the current densities in V_i can be derived as:

$$\vec{E}_i^{scat}\left(\vec{J}_{eq}, \vec{M}_{eq}\right) = \eta_i \mathbf{L}_i\left(\vec{J}_{eq}\right) - \mathbf{K}_i\left(\vec{M}_{eq}\right) \tag{27}$$

$$\vec{H}_i^{scat}\left(\vec{J}_{eq}, \vec{M}_{eq}\right) = \mathbf{K}_i\left(\vec{J}_{eq}\right) + \eta_i^{-1} \mathbf{L}_i\left(\vec{M}_{eq}\right) \tag{28}$$

where,

$$\mathbf{L}_i\left(\vec{X}_{eq}\right) = -jk_i \int_{\Omega'} \left[\bar{\bar{I}} + \frac{1}{k_i^2} \nabla\nabla\cdot\right] \vec{X}_{eq}\left(\vec{r}'\right) G_i\left(\vec{r}, \vec{r}'\right) d\Omega' \tag{29}$$

$$\mathbf{K}_i\left(\vec{X}_{eq}\right) = \int_{\Omega} \nabla \times G_i\left(\vec{r}, \vec{r}'\right) \vec{X}_{eq}\left(\vec{r}'\right) d\Omega' \tag{30}$$

where Ω is a surface for a surface integral and a volume for a volume integral, $\bar{\bar{I}}$ is the idem factor, or unit dyad, and $G_i\left(\vec{r}, \vec{r}'\right)$ is the Green function for a homogeneous space with material profile $(\varepsilon_{ih}, \mu_{ih})$:

$$G_i(\vec{r},\vec{r}') = \frac{e^{-jk_i|\vec{r}-\vec{r}'|}}{4\pi|\vec{r}-\vec{r}'|} \tag{31}$$

and $k_i = \omega\sqrt{\varepsilon_{ih}\mu_{ih}}$.

Appropriate integral equations must be posed to solve for the unknown equivalent current densities. Consider a material surface $S_{i,j}$ separating two material regions. From (22) and (23), the fields must satisfy the boundary constraints:

$$\hat{n}_i \times \vec{E}_i^{inc}\Big|_{S_{i,j}^+} = -\vec{M}_{i,j} - \hat{n}_i \times \vec{E}_i^{scat}\Big|_{S_{i,j}^+} \tag{32}$$

$$-\hat{n}_i \times \vec{E}_j^{inc}\Big|_{S_{i,j}^-} = \vec{M}_{i,j} + \hat{n}_i \times \vec{E}_j^{scat}\Big|_{S_{i,j}^-} \tag{33}$$

$$\hat{n}_i \times \vec{H}_i^{inc}\Big|_{S_{i,j}^+} = \vec{J}_{i,j} - \hat{n}_i \times \vec{H}_i^{scat}\Big|_{S_{i,j}^+} \tag{34}$$

$$-\hat{n}_i \times \vec{H}_j^{inc}\Big|_{S_{i,j}^-} = -\vec{J}_{i,j} + \hat{n}_i \times \vec{H}_j^{scat}\Big|_{S_{i,j}^-} \tag{35}$$

where $\vec{E}_i^{inc}, \vec{H}_i^{inc}$ are radiated by impressed sources in V_i, $\vec{E}_i^{scat}, \vec{H}_i^{scat}$ are radiated by equivalent currents in volume V_i (similarly in V_j), and $\hat{n}_j = -\hat{n}_i$ has been assumed. It is also noted, that on $S_{i,j}^-$, the equivalent currents in V_j contributing to $\vec{E}_j^{scat}, \vec{H}_j^{scat}$ are $-\vec{J}_{i,j}$ and $-\vec{M}_{i,j}$.

The constraints on the interior and exterior boundaries in (32) - (35) are used to formulate the integral equation for material boundaries. These equations can be combined since only two constraints are needed to solve for the two unknowns. They must be combined in a manner that avoids spurious "interior resonances." Two options are available within *Mat-Scat*. The first is the classical PMCHWT technique [23, 24]. This is equivalent to adding (32) with (33) and (34) with (35), which leads to:

$$\hat{n}\times\vec{E}_i^{inc}\Big|_{S_{i,j}^+} - \hat{n}\times\vec{E}_j^{inc}\Big|_{S_{i,j}^-} = -\hat{n}\times\vec{E}_i^{scat}\Big|_{S_{i,j}^+} + \hat{n}\times\vec{E}_j^{scat}\Big|_{S_{i,j}^-}, \tag{36}$$

$$\hat{n}\times\vec{H}_i^{inc}\Big|_{S_{i,j}^+} - \hat{n}\times\vec{H}_j^{inc}\Big|_{S_{i,j}^-} = -\hat{n}\times\vec{H}_i^{scat}\Big|_{S_{i,j}^+} + \hat{n}\times\vec{H}_j^{scat}\Big|_{S_{i,j}^-}. \tag{37}$$

It is observed that the diagonal terms cancel. The diagonal terms resulting from the residuals of the principal value integrals of the **K** operators also cancel. Thus, the PMCHWT is a first-kind integral equation. Furthermore, due to the $\nabla\nabla$ term of the **L**-operator, the PMCHWT has a hypersingular kernel. A consequence of this is that the operator is not expected to be mesh stable. That is, as the discretization is continually refined – increasing accuracy – the condition number of the discretized operator will grow. However, because of the $\nabla\nabla$ term, the PMCHWT operator explicitly represents the quasi-static field affects, and it can be expected to model objects with geometric singularities well.

We can also look at another interesting property of the PMCHWT operator. Consider the situation when $\mathrm{Im}(\varepsilon_j) \to -j\infty$, that is the limit that the material body becomes a PEC. It can be shown that in this limit, (36) will reduce identically to the EFIE and (37) will reduce to the MFIE in. Also, consider the limit that $\varepsilon_j \to \infty$. In this limit, the boundary becomes a hard electric

boundary, and the fields in V_j will tend to 0, and $\vec{M}_{i,j} \to 0$. It can be shown that in this limit, the operators in (36) and (37) are bounded. Consequently, the PMCHWT operator is stable relative to the refractive index of the material object.

The second option available within *Mat-Scat* is a Müller formulation [25]. This formulation is derived by weighting (32) by ε_{ib}, (33) by $-\varepsilon_{jb}$ and adding the equations to obtain:

$$\hat{n}_i \times \varepsilon_{ib}\vec{E}_i^{inc}\Big|_{S_{i,j}^+} + \hat{n}_i \times \varepsilon_{jb}\vec{E}_j^{inc}\Big|_{S_{i,j}^-} = -\vec{M}_{i,j}\left(\varepsilon_{ib}+\varepsilon_{jb}\right) - \hat{n}_i \times \varepsilon_{ib}\vec{E}_i^{scat}\Big|_{S_{i,j}^+} - \varepsilon_{jb}\,\hat{n}_i \times \vec{E}_j^{scat}\Big|_{S_{i,j}^-} \tag{38}$$

Dually, (34) is weighted by μ_{ib}, and (35) by $-\mu_{jb}$ and adding them, leading to:

$$\hat{n}_i \times \mu_{ib}\vec{H}^{inc}\Big|_{S_{i,j}^+} + \hat{n}_i \times \mu_{jb}\vec{H}^{inc}\Big|_{S_{i,j}^-} = \vec{J}_{i,j}\left(\mu_{ib}+\mu_{jb}\right) - \hat{n}_i \times \mu_{ib}\vec{H}^{scat}\Big|_{S_{i,j}^+} - \hat{n}_i \times \mu_{jb}\vec{H}^{scat}\Big|_{S_{i,j}^-} \tag{39}$$

The **K**-operator requires a principal value integral, which leads to a well known residue plus the principal value. After performing the principal value integral, (38) and (39) are written as:

$$\hat{n}_i \times \varepsilon_{ib}\vec{E}_i^{inc}\Big|_{S_{i,j}^+} + \hat{n}_i \times \varepsilon_{jb}\vec{E}_j^{inc}\Big|_{S_{i,j}^-} = -\frac{1}{2}\vec{M}_{i,j}\left(\varepsilon_{ib}+\varepsilon_{jb}\right) - \hat{n}_i \times \varepsilon_{ib}\vec{E}_i^{scat}\Big|_{S_{i,j}^+} - \hat{n}_i \times \varepsilon_{jb}\vec{E}_j^{scat}\Big|_{S_{i,j}^-} \tag{40}$$

$$\hat{n}_i \times \mu_{ib}\vec{H}^{inc}\Big|_{S_{i,j}^+} + \hat{n}_i \times \mu_{jb}\vec{H}^{inc}\Big|_{S_{i,j}^-} = \frac{1}{2}\vec{J}_{i,j}\left(\mu_{ib}+\mu_{jb}\right) - \hat{n}_i \times \mu_{ib}\vec{H}^{scat}\Big|_{S_{i,j}^+} - \hat{n}_i \times \mu_{jb}\vec{H}^{scat}\Big|_{S_{i,j}^-} \tag{41}$$

where, the surface integrals over $S_{i,j}$ use the modified **K** integral:

$$\tilde{\mathbf{K}}_k \cdot \vec{X}_{eq} = \oint_{S_{i,j}} \nabla \times G_k\left(\vec{r},\vec{r}'\right)\vec{X}_{eq}\left(\vec{r}'\right)d\Omega' \tag{42}$$

where $\vec{r} \in S_{i,j}$ and $k = i$ or j.

It was observed by Müller that for this combined form, the hypersingular static terms arising from the **L**-operators will cancel with vanishing separation of the source and observation points ([25], pg. 300). Thus, the effective singularity of the combined operator is only $1/R$. Consequently, the Müller formulation is a second-kind integral equation that consists of a diagonal term plus a compact operator. As a consequence, the Müller formulation is expected to be well conditioned and mesh stable – that is the condition number will tend to a constant with increased mesh discretization. Since the kernel is not hypersingular, one can also expect that for smooth material bodies, the LCN method will converge exponentially, and to exhibit a rate of convergence superior to the PMCHWT formulation. A caveat is that in the instance where $\varepsilon_j >> \varepsilon_i$, or $\mu_j >> \mu_i$, the integral equations in volume V_j are amplified by the constitutive relations. As a consequence, for high contrast materials, the error in the Müller formulation is amplified.

In general, the Müller formulation is more accurate for moderate to low contrast materials ($\varepsilon_r < 20$), and the PMCHWT formulation is more accurate for high-contrast materials

Next, a on a conductor surface, one can constrain the total tangential electric field to be zero on the surface, leading to the familiar electric field integral equation (EFIE) [22]:

$$\hat{n}_i \times \vec{E}_i^{inc}\Big|_{S_{i,p}^+} = -\hat{n}_i \times \vec{E}_i^{scat}\Big|_{S_{i,p}^+} \tag{43}$$

The magnetic field is also constrained on a PEC surface using (25), leading to the magnetic field integral equation (MFIE) [22]:

$$\hat{n}_i \times \vec{H}_i^{inc}\Big|_{S_{i,p}^+} = \vec{J}_{i,p} - \hat{n}_i \times \vec{H}_i^{scat}\Big|_{S_{i,p}^+} \tag{44}$$

The linear combination of the EFIE and MFIE is referred to as the combined field integral operator (CFIE), which can be expressed as [22]:

$$\begin{aligned} &\alpha_{CFIE}\,\vec{t}\cdot\vec{E}_i^{inc}\Big|_{S_{i,p}} + (1-\alpha_{CFIE})\,\eta_i\,\vec{t}\cdot\hat{n}\times\vec{H}_i^{inc}\Big|_{S_{i,p}} = \\ &\alpha_{CFIE}\left(-\vec{t}\cdot\vec{E}_i^{scat}\Big|_{S_{i,p}}\right) + (1-\alpha_{CFIE})\,\eta_i\vec{t}\cdot\left(\vec{J}_{i,p} - \hat{n}\times\vec{H}_i^{scat}\Big|_{S_{i,p}}\right). \end{aligned} \tag{45}$$

where α_{CFIE} is a real constant, generally defined between 0 and 1, and $\vec{t}$ is a vector tangential to the PEC surface $S_{i,p}$. When α_{CFIE} = 0, this reduces to the EFIE, and when α_{CFIE} = 1, this reduces to the MFIE.

Next, in regions where the volume currents are non-zero, an additional constraint is levied.

$$\vec{E}_i(\vec{r})\Big|_{\vec{r}\in V_i} = \vec{E}_i^{scat}(\vec{r}) + \vec{E}_i^{inc}(\vec{r}) \tag{46}$$

$$\vec{H}_i(\vec{r})\Big|_{\vec{r}\in V_i} = \vec{H}_i^{scat}(\vec{r}) + \vec{H}_i^{inc}(\vec{r}) \tag{47}$$

Given the volume currents defined in (26), (46) and (47) can be restated as:

$$\vec{E}_i^{inc}(\vec{r})\Big|_{\vec{r}\in V_i} = \frac{\vec{J}_V(\vec{r})}{j\omega\varepsilon_o\varepsilon_{ib}\left(\frac{\varepsilon_{ir}}{\varepsilon_{ib}} - 1\right)} - \vec{E}_i^{scat}(\vec{r}) \tag{48}$$

$$\vec{H}_i^{inc}(\vec{r})\Big|_{\vec{r}\in V_i} = \frac{\vec{M}_V}{j\omega\mu_o\mu_{ib}\left(\frac{\mu_{ir}}{\mu_{ib}} - 1\right)} - \vec{H}_i^{scat}(\vec{r}). \tag{49}$$

Note that (48) and (49) are only constrained in regions where $\vec{J}_V \neq 0$ or $\vec{M}_V \neq 0$. The scattered field is due to all equivalent currents present in V_i.

Combining (36), (37) (or (38) and (39)), (45), (48), and (49) leads to a highly versatile integral formulation from which the general treatment of the electromagnetic scattering of arbitrarily inhomogeneous material scatterers can be applied. The introduction of the background material within each material volume can automatically eliminate volume cells in large homogenous regions. It also can lead to a better conditioned formulation when simulating high contrast materials. This formulation is also directly applicable to anisotropic media.

A computer code based on this integral formulation has been developed. The code is referred to as *Mat-Scat* for general "material scattering." The code has been fully validated for surface and volume scattering using curvilinear quadrilateral and hexahedral cell discretization. The code can handle an arbitrary number of material regions. Also, either the PMCHWT or the Müller formulation can be applied to a material surface boundary. The software also utilizes

curvilinear meshing of arbitrary order. Mixed-order basis functions are used to expand the current densities. While the basis order can be arbitrarily high, practically speaking, the highest order that has been simulated has been 17^{th} order. The software is written in FORTRAN, and is platform independent.

4.C.2 Validation

The University of Kentucky *Mat-Scat* software has been validated for a number of canonical and non-canonical geometries. In this section, a representative set of validating results are presented.

4.C.2.1 Scattering by Material Spheres

Initially, consider the scattering by a PEC sphere that is coated with a thin dielectric shell. The PEC sphere has a radius a defined by $k_o a = 3.5$. The dielectric coating has a relative permittivity of $\varepsilon_r = 4 - j0.1$ and an outer radius b defined by $k_o b = 3.8$. The integral equation solution employed Müller's formulation for the dielectric boundary, and the CFIE with $\alpha = 0.2$ for the PEC boundary. Two meshes were used to simulate this problem. The first used a total of 48 7^{th}-order quadrilateral cells to model both the PEC/dielectric boundary and the dielectric/air boundary. The second mesh used a total of 108 7^{th} order quadrilateral cells. For each mesh, the order of basis was increased from 2 to 6. Table 1 presents the mean error, total CPU time, and the condition number estimate for the LCN solution employing either the polynomial complete or the mixed-order basis functions for the two meshes. In this table, P is the basis order, N_c is the total number of quadrilateral cells, and N is the total number of degrees of freedom (also, the rank of the matrix). For all discretizations the mixed-order basis exhibits improved solution error as compared to the polynomial complete basis. It is observed that the condition number resulting from the polynomial complete basis is much larger than that recorded for the mixed-order basis. This is predominately due to the fact that the polynomial complete formulation is not charge conserving, and the spurious charges in the solution introduce small singular values in the system matrix.

Table 1 Scattering by a dielectric coated PEC sphere with PEC sphere radius $k_o a$ = 3.5, and outer shell radius $k_o a$ = 3.8 computed with polynomial complete (P. C.) and mixed-order (M. O.) basis functions.

		N		Mean Error		CPU-s		Condition #	
P	N_c	P. C.	M.O.	P. C.	M.O.	P. C.	M.O.	P. C.	M.O.
2	48	1296	864	0.49	0.29	98	69	123	45
4	48	3600	2280	$2.1\text{x}10^{-2}$	$6.2\text{x}10^{-3}$	362	318	8711	48
6	48	7056	6048	$3.4\text{x}10^{-3}$	$3.1\text{x}10^{-4}$	1965	985	10377	51
2	108	2916	1944	$5.8\text{x}10^{-2}$	0.10	231	190	126	43
3	108	5184	3888	$2.5\text{x}10^{-2}$	$6.7\text{x}10^{-3}$	614	406	835	47
4	108	8100	6480	$3.6\text{x}10^{-3}$	$1.0\text{x}10^{-3}$	2392	979	6217	49

Another example of a dielectric coated metal sphere is considered. A 10 cm radius PEC sphere is coated by a 1 cm thick spherical dielectric shell with relative permittivity $\varepsilon_r = 9 - j0.3$. The sphere is illuminated by a plane wave at 1 GHz (effective radii of $k_o a = 2.1$, $k_o b = 2.3$). This case was modeled using a combined CFIE/SIE formulation using either the PMCHWT SIE formulation or the Müller formulation, and CFIE/VIE formulations. For the CFIE/SIE formulation, a total of 48 curvilinear quadrilateral cells were employed, 24 on the PEC surface, and 24 on the dielectric surface. For the CFIE/VIE formulation, a total of 48 curvilinear cells were also used, 24 curvilinear quadrilaterals on the PEC surface, and 24 curvilinear hexahedron were used to model the dielectric shell. The error versus the number of unknowns was recorded as the basis order was increased. It is observed that for this case, the CFIE/Müller formulation was superior in terms of computational cost. However, the CFIE/VIE outperformed the CFIE/PMCHWT formulation. This is generally true for homogeneous material problems with moderately low contrast materials.

To study this somewhat further, consider the case of the scattering by a dielectric sphere. The radius of the sphere is 10 cm. The electromagnetic scattering was predicted at f = 2 GHz ($\lambda_o \approx 15\text{cm}, k_o a = 4.2$), when the sphere had two different relative permittivities: $\varepsilon_r = 1.2$ and $\varepsilon_r = 36 - 0.3j$. The surface of the sphere was discretized into 54 high-order curvilinear quadrilateral cells (8^{th} order isoparametric cells). The discretization was then refined by increasing the order of the basis functions (p-refinement). The RMS error in the RCS predicted by the LCN simulation versus the total of unknowns is illustrated in Fig. 8(a) for $\varepsilon_r = 1.2$ when the basis order is increased from 2^{nd}-order through 6^{th}-order. Similarly, the RMS error in the RCS for $\varepsilon_r = 36 - 0.3j$ is illustrated in Fig. 8(b), as the basis order is increased from 2^{nd} to 7^{th}-order. (Note that the total number of unknowns for p^{th}-order mixed-order basis functions is: $(p+1) \times p \times 4 \times N_c$, where in this example $N_c = 54$ cells [5]). For the low-contrast sphere (Fig. 8(a)), both methods are converging exponentially. However, the Müller method is converging at a faster rate sine the PMCHWT operator has a hypersingular kernel. Over the whole range, the Müller method is also at a much lower level. For the higher contrast dielectric sphere (Fig. 8(b)), the Müller method again exhibits a faster rate of convergence. However, the level of error is higher for coarser discretizations. Consequently the PMCHWT formulation reaches 2 digits of accuracy with fewer unknowns than the Müller formulation. Due to the rapid convergence, the Müller formulation is more efficient if additional digits of accuracy are needed.

The condition number of the matrices studied in the examples of Figs. 8(a) and 8 (b) are illustrated in Fig. 9. (The condition numbers reported were computed as the ratio of the maximum to minimum singular values of the impedance matrix.) As expected, the Müller method is stable relative to discretization due to the properties of the second-kind integral operator. The condition number resulting from the PMCHWT algorithm grows linearly with discretization on the log-log plot. This is due to the hypersingular kernel from the **L** operator.

This same example was also studied for an h-refinement. That is, the order of the basis functions were held fixed at third order and the mesh was refined.. The RMS error in the RCS is illustrated in Fig. 10 for both the cases when $\varepsilon_r = 1.2$ and $\varepsilon_r = 36 - 0.3j$. On the log-log scale, the Müller formulation leads to third-order convergence, which is exactly what is expected of the third-order basis functions. Optimal convergence is expected for this smooth geometry since the operator is a second-kind operator. On the other hand, the PMCHWT formulation converges approximately with $O\left(h^{1.5}\right)$. The reduction in error convergence is due to the hypersingularity of the kernels, and the additional derivatives that are effectively applied to the basis functions.

Again, for the low contrast sphere, the Müller formulation is the most efficient. Whereas for the high-contrast sphere, the PMCHWT formulation is more efficient for coarser discretizations, and crosses over with the Müller formulation at 3 digits.

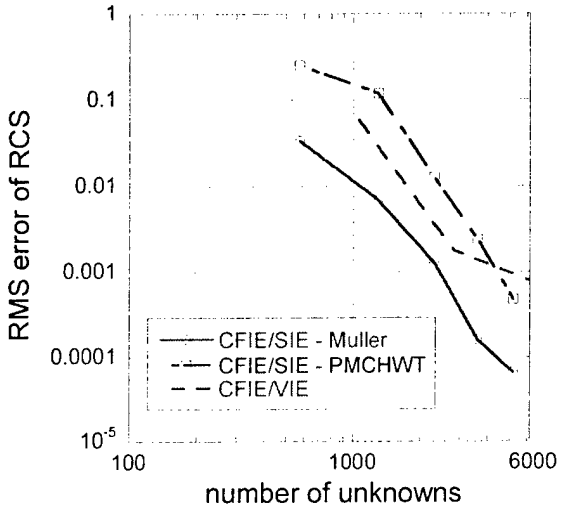

Fig. 7 RMS error in the RCS of a dielectric coated PEC sphere ($\varepsilon_r = 9 - j0.3$) and $k_o a = 2.1$, $k_o b = 2.3$

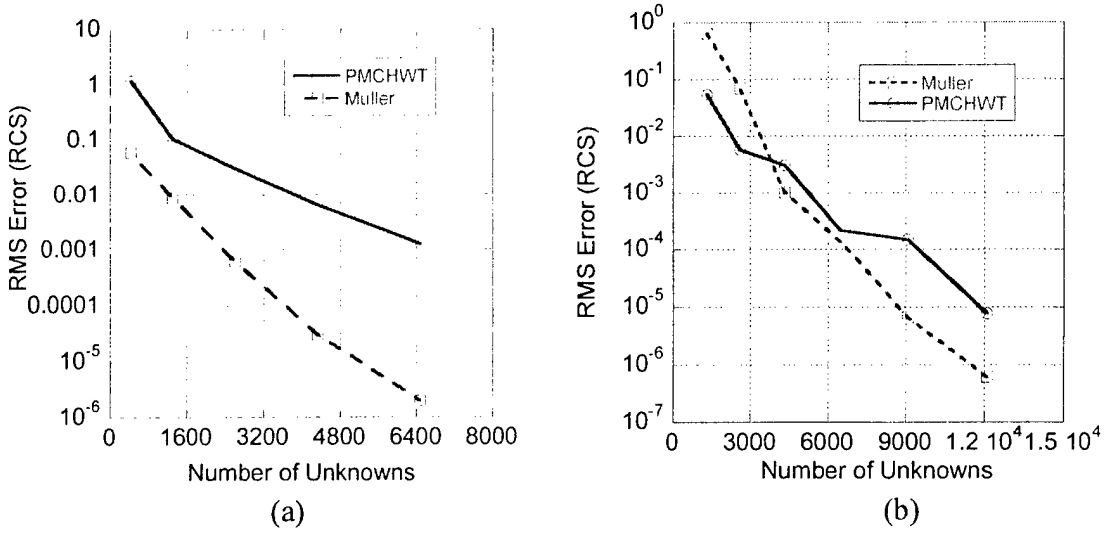

Fig. 8 RMS error in the bi-static RCS for the scattering by a dielectric sphere versus the total number of unknowns based on calculations made via the LCN discretization of the Müller, PMCHWT, and PMCHWT-minus (PMCHWT-) formulations. (a) $\varepsilon_r = 1.2$ (b) $\varepsilon_r = 36 - 0.3j$.

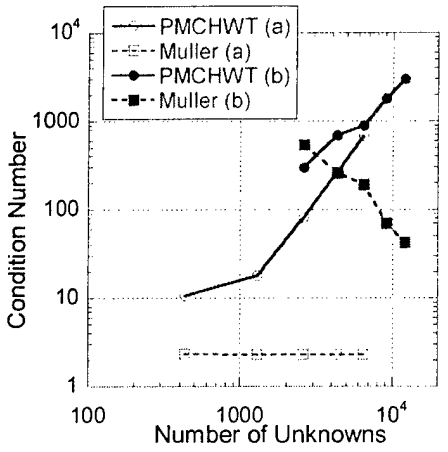

Fig. 9 Condition number of the matrix arising from the LCN discretizationc of the dielectric sphere with the PMCHWT or the Muller formulation versus the total number of unknowns for increasing order and: (a) $\varepsilon_r = 1.2$ (b) $\varepsilon_r = 36 - 0.3j$.

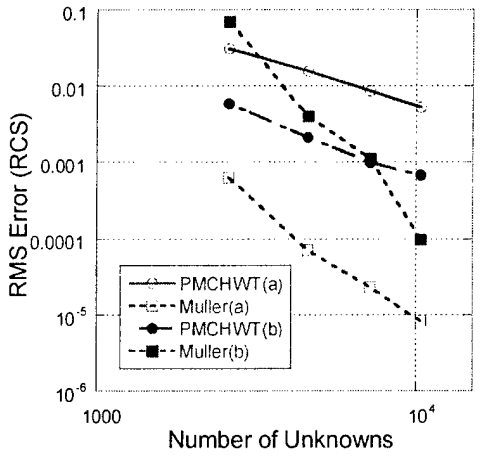

Fig. 10 RMS error of the RCS for the dielectric sphere for fixed order (p = 3) and increasing number of cells when (a) $\varepsilon_r = 1.2$ (b) $\varepsilon_r = 36 - 0.3j$.

4.C.2.2 EMCC Targets

A number of the EMCC Targets have been simulated using *Mat-Scat* to validate the accuracy and efficiency of the software. A number of those are reviewed here.

Initially, consider the EMCC wedge cylinder plate (Fig. 11 (a)). The plate lies in the $z = 0$ plane and the center axis of the plate (through the tip) is aligned along the x-axis. The

curvilinear mesh used to represent the geometry is illustrated in Fig. 11 (a). Note that curvilinear cells were only needed near the curved circular boundary. Linear quadrilaterals were used to model the remainder of the target. The monostatic RCS at an elevation of 10° off the $z = 0$ plane ($\theta = 80°$) as calculated via the LCN solution of the EFIE using mixed-order basis functions is presented in Fig. 11 (b). These results can be compared to measured results and computed results published by Woo, et al., in [26] and reproduced in Fig. 11 (c). Excellent agreement is seen, even for the lowest order. The CPU time and problem dimensions are recorded in Table 2. The CPU times were recorded on a single 750 MHz HP-PA RISC processor. The total CPU time includes the calculation of 180 solution vectors (1 degree spacing).

Next, consider the EMCC metallic single ogive [27]. The single ogive target has a half angle of 22.62 degrees, a total length of 10 inches, and a maximum radius of 1 inch. The major axis of the ogive is aligned along the x-axis. The ogive approximated by 72 seventh-order curvilinear quadrilaterals is illustrated in Fig. 12 (a). The monostatic RCS predicted using the LCN method is illustrated in Fig. 12(b) for a frequency $f = 1.18$ GHz, and in Fig. 13 (a) for $f = 9$ GHz. In both cases, the RCS was sampled in the $\theta = 90°$ plane with 1 degree increments in ϕ. These results can be compared with measured data and independent computations published in [27], and reproduced in Fig. 12 (c) for $f = 1.18$ GHz, and Fig. 13 (b) for $f = 9$ GHz. Excellent agreement is observed. At $f = 9$ GHz, the ogive is approximately 7.6 λ_o in length and 0.76 λ_o in radius. This was modeled with 288 cells with $p+1 = 4$ and polynomial complete basis. This lead to a total of only 9,216 unknowns. The total fill time was 839 s on a single 750 MHz HP PARISC processor. The factor and solve time for 180 angles was 1,278 s.

The next case studied was the EMCC metallic double ogive, illustrated in Fig. 14 (a). The left half of the ogive has a half angle of 46.4 degrees at the tip and a half length of 2.5 inches. The maximum radius of the half ogive is 1 inch. The right half of the ogive has a half angle of 22.62 degrees at the tip, a half length of 5 inches, and a maximum radius of 1 inch (where the two half ogives meet). The ogive was aligned along the x-axis. The monostatic RCS was again computed via the LCN method. A graph of the RCS versus ϕ computed in the $\theta = 90°$ plane is illustrated in Fig. 14 (b) at $f = 1.57$ GHz, and in Fig. 15 (a) at $f = 9$ GHz. Note that $\phi = 0$ corresponds to the plane wave directed at the 22.62 degree tip. The results are to be compared to measured data and independent calculations published in [27] and reproduced in Figs. 14 (c) for 1.57 GHz and 15 (b) at 9 GHz. Again, excellent agreement is realized.

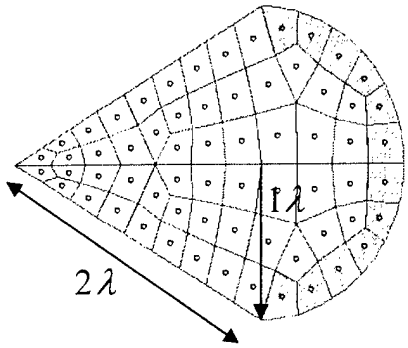

(a)

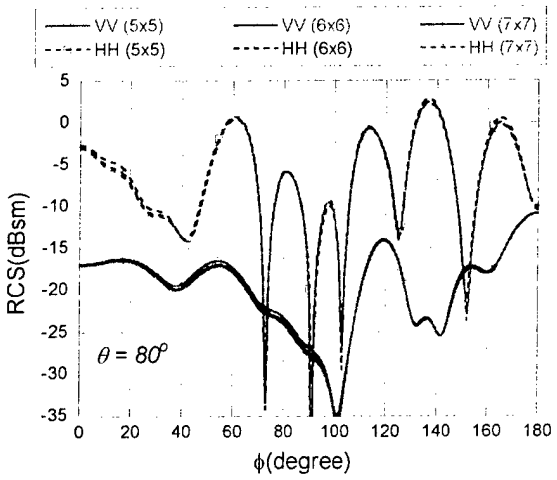

(b)

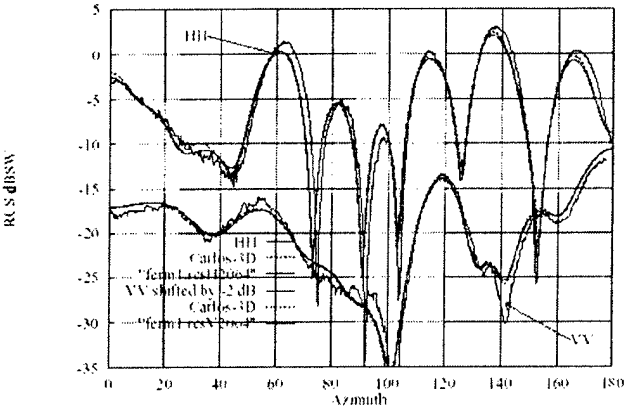

(c)

Fig. 11 EMCC wedge cylinder plate, (a) curvilinear cell discretization, (b) RCS computed via the LCN method with mixed-order basis for p+1 = 5, 6, and 7, and, (c) results from [26].

# cells	*p+1*	N	Fill	Total CPUs
64	5	2,560	197.3 s	245.5 s
64	6	3,840	408.0 s	535.2 s
64	7	5,376	696.8 s	996.0 s

Table 2. Dimension and Computation Time for the EMCC Wedge Cylinder Plate (CPU time recorded on a single 750 MHz HP-PARISC processor)

Next, the RCS of the metallic double ogive coated by a thin lossy dielectric coating was analyzed. The geometry is illustrated in Fig. 16 (a). The coating was added on by extending the surface of the double ogive by 10 % along the surface normal. Thus, the maximum radius of the coating is 1.1 inches. The left half length of the coated ogive is 2.75 inches, and the right half length of the coated ogive is 5.5 inches. The coating was assumed to be isotropic homogenous with a relative permittivity $\varepsilon_r = 9 - j0.3$. The monostatic RCS computed in the $\theta = 90°$ plane

is illustrated in Fig. 16 (b) as computed via the LCN with a combined field surface integral equation formulation, as defined in Section 2.1. For this discretization, the RCS has converged to < 1 % accuracy with fourth order basis.

Next, the RCS of the NASA Almond is studied [27]. The NASA almond is a challenging structure in that the geometry is singular at the two tips and there is a high-rate of curvature in the geometry. An example of a curvilinear mesh used to model the almond is illustrated in Fig. 17 (a). The monostatic RCS of the almond was computed in the zero elevation plane ($\theta = 90°$) as a function of the azimuthal angle ϕ. The broad side of the almond lies in this plane, and $\phi = 0°$ corresponds to incidence on the sharp tip. The RCS of the Almond predicted by the LCN method at 7 GHz. The LCN simulation employed a 140-cell eighth-order curvilinear mesh and mixed-order basis. The RCS predicted by *Mat-Scat* is illustrated in Fig. 17 (b) for horizontal polarization (HH) for fifth and sixth-order discretizations, requiring 5,600 and 8,400 unknowns, respectively. The difference between these two simulations is < .001 dB. A Galerkin simulation employing low-order basis functions was also used to simulate the Almond. The Galerkin simulation utilized a mesh consisting of 21,120 bi-linear quadrilaterals, supporting 31,680 zeroth-order divergence conforming GWP_0 basis functions. The low-order Galerkin simulation still has not converged for angles of incidence near the tips of the almond, whereas the LCN solution has converged with far fewer unknowns. Figure 17(c) compares the RCS as predicted by the LCN solution of the CFIE with mixed-order basis versus that computed with polynomial-complete basis functions. Both simulations used the same discretization as that in Fig. 7 and sixth-order basis functions. The polynomial complete basis still results in significant error for incidence near the tips. These results can be compared against measured data and independent computations published by Woo et al. in [27], and reproduced in Fig. 17 (d).

Finally, consider the case of the thick trapezoidal plate [28, 29] coated along the edges with a thin dielectric coating (see Fig. 18). This geometry has also been referred to as the EMCC Dart. The base of the PEC plate is 7 feet long and 3 feet high. The top of the plate is 3 feet long. The plate is 1 inch thick. The edge of the plate is coated with uniform dielectric coating with relative permittivity $\varepsilon_r = 4.5 - j9$. The coating is 2 inches wide (except at the corners) and is 1 inch thick. The plate and coating were modeled with a total of 158 bi-linear quadrilaterals. The plate is situated in the z = 0 plane. The monostatic RCS of the plate was computed via the LCN method with mixed-order basis in the zero degree elevation plane ($\theta = 90°$). The angle $\phi = 0°$ represents incidence on the sharp tip of the plate. The RCS is illustrated in Figs. 19 (a) and (b). These results can be compared to Fig. 7 of [29]. The vertical polarization converges quite well for order q = 5 (N = 9,200). Whereas, the horizontal polarization requires q = 6 for convergence (N = 13,800).

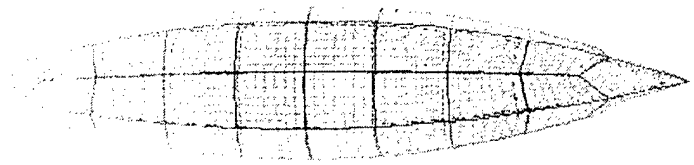

(a)

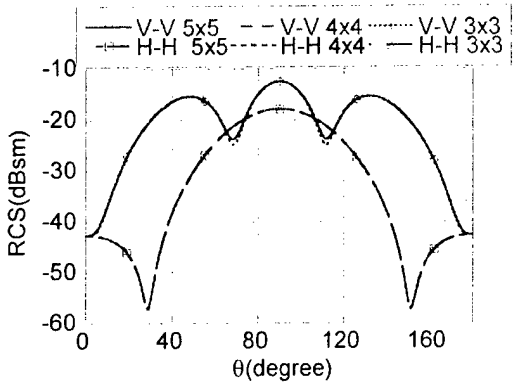

(b)

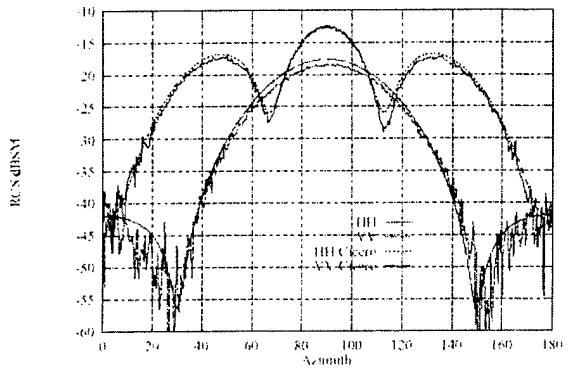

(c)

Fig. 12 EMCC metallic single ogive, f = 1.18 GHz. (a) Patch discretization – 72 seventh-order curvilinear cells, (b) RCS computed via the LCN method for p+1 = 3, 4, and 5, (c) results from [27].

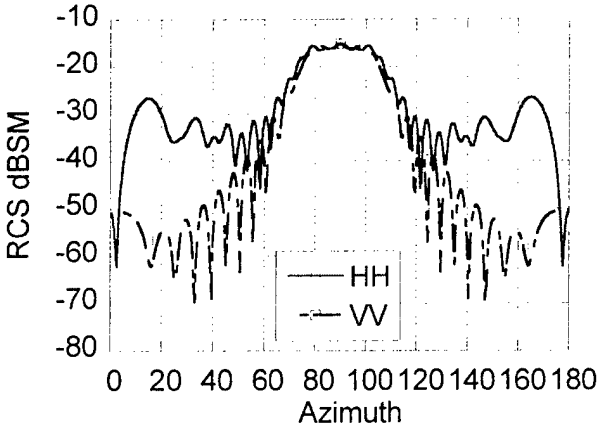

(a)

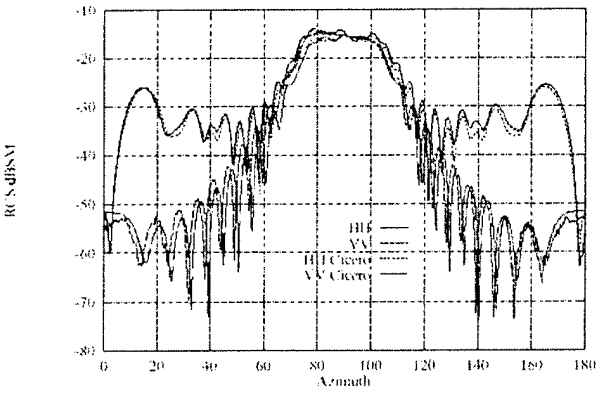

(b)

Fig. 13 EMCC metallic single ogive, f = 9 GHz, (a) RCS computed via the LCN method for p+1 = 4, and 288 seventh-order curvilinear cells, (b) results from [27].

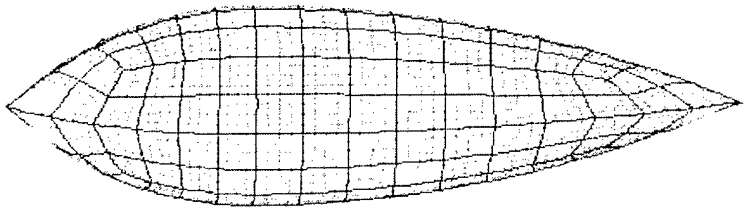

(a)

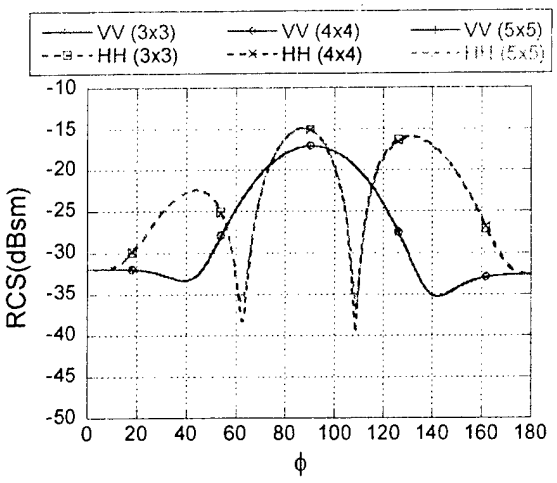

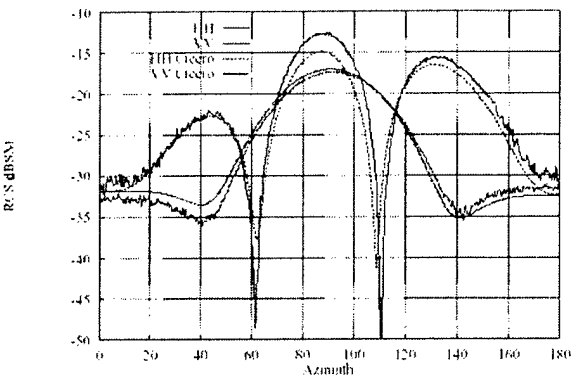

(b) (c)

Fig. 14 EMCC metallic double ogive, f = 1.57 GHz, (a) discretization with 56 seventh-order curvilinear cells, (b) RCS computed via the LCN method for p+1 = 4, and, (c) results from [27].

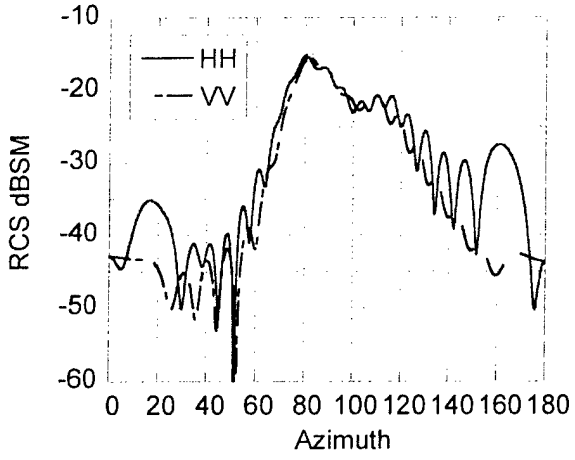

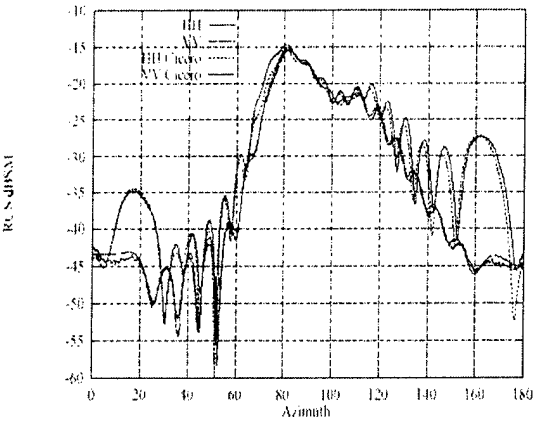

Fig. 15 EMCC metallic double ogive, f = 9 GHz, (a) RCS computed via the LCN method with 224 cells and p+1 = 4, (b) results from [27].

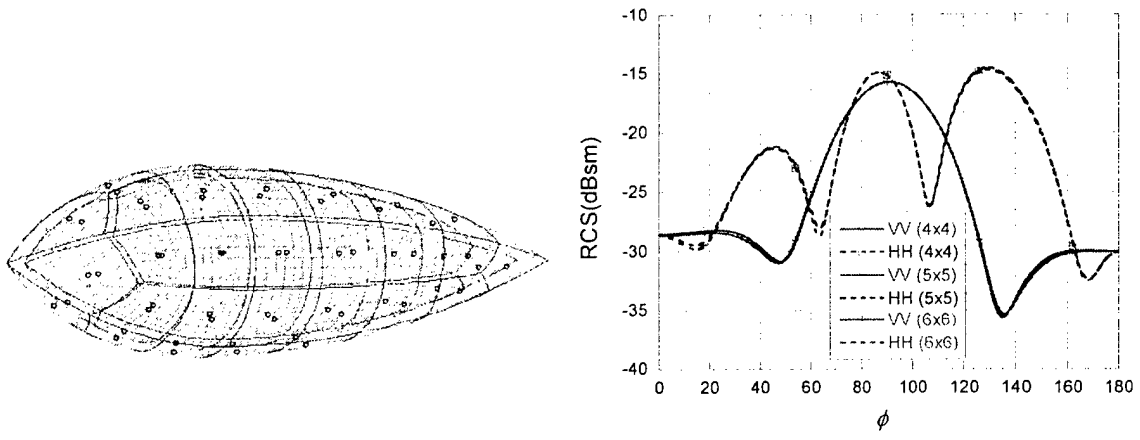

(a) (b)

Fig. 16 Coated EMCC metallic double ogive, f = 1.57 GHz. Coated with thin dielectric coating with $\varepsilon_r = 9 - j0.3$. (a) Curvilinear discretization. (b) RCS (monostatic) computed in the $\theta = 90°$ plane via the LCN method for p+1 = 4, 5, and 6.

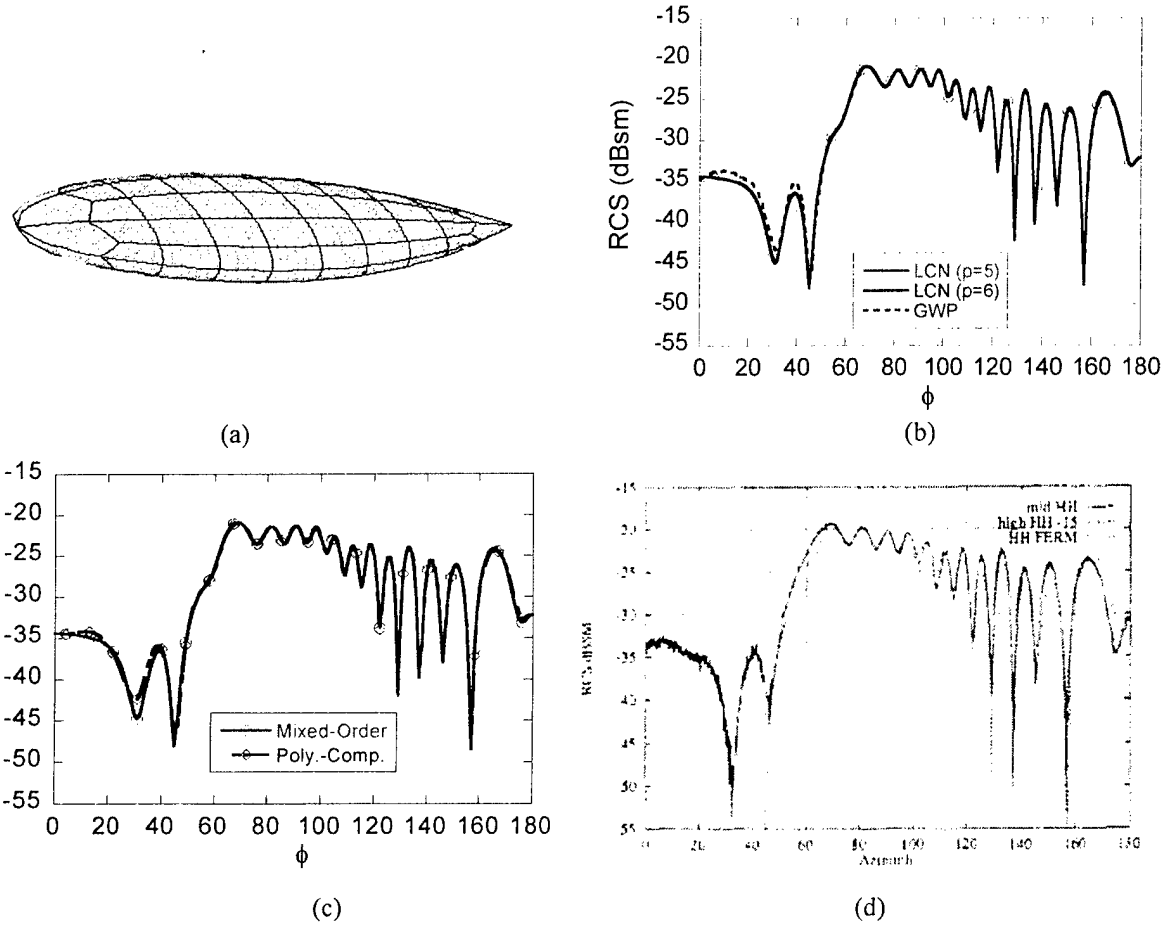

(a) (b)

(c) (d)

Fig. 17 NASA Almond, f = 7 GHz, (a) discretization, (b) RCS computed via the LCN method for p+1 = 3 via the CFIE and MFIE with polynomial complete basis as well as a Galerkin scheme with RWG basis (HH), and, (c) LCN method with p = 5 via the EFIE with mixed-order basis as compared to a Galerkin method with RWG basis (HH), (d) results from [27].

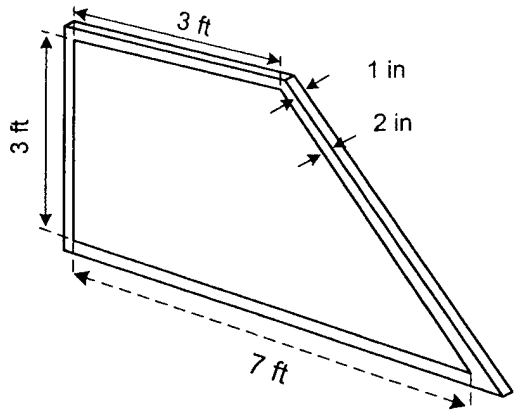

Fig. 18 Coated trapezoidal plate – 0.0254 m thick PEC plate with a 0.0508 m dielectric edge coating $\varepsilon_r = 4.5 - j9$. The plate is located in the $z = 0$ plane.

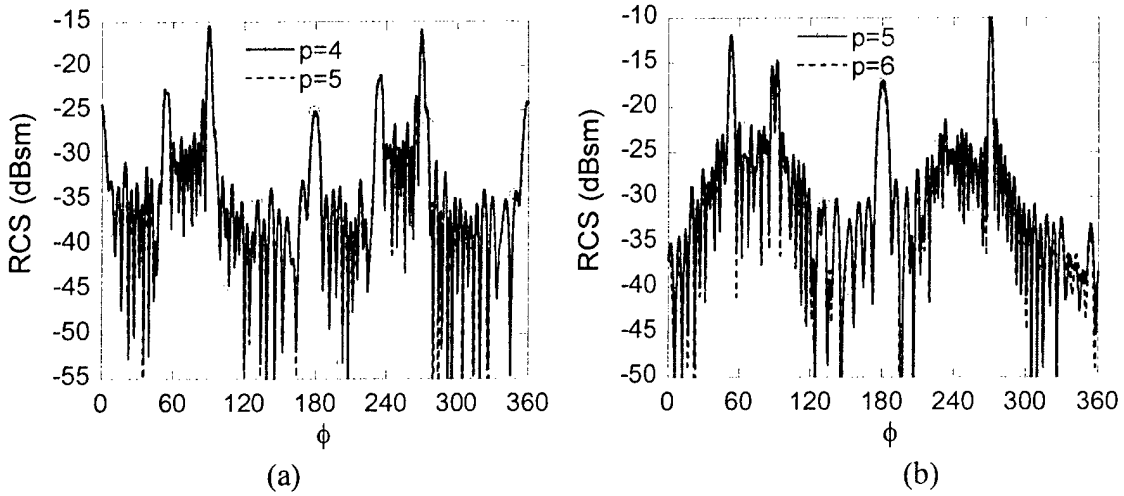

Fig. 19 Monostatic RCS of the coated trapezoidal plate computed via the LCN method in the zero elevation plane at 1 GHz. (a) V-V polarization, (b) H-H polarization.

4.D Fast Solution Methods

4.D.1 The Quadrature Sampled Pre-Corrected FFT Algorithm

We have developed a novel fast, high-order solution procedure referred to as the Quadrature Sampled Pre-Corrected FFT (QS-PCFFT). The method accelerates far-interaction terms of an integral operator using the discontinuous FFT [30], which combines Gaussian-quadrature integration with the FFT. We have applied the method to our high-order method of moment scheme with point-based discretization (equivalent to the locally corrected Nyström) for electromagnetic scattering. This is briefly described in the following.

Consider the electromagnetic scattering by a PEC object. The electric field integral equation (EFIE) can be used to solve for the currents induced on the PEC surface S. The EFIE is described as:

$$\mathbf{E}^i(\mathbf{r}) = \iint_S \bar{\bar{G}}(\mathbf{r},\mathbf{r}') \cdot \mathbf{J}(\mathbf{r}')\, d\mathbf{r}' \tag{50}$$

where $\mathbf{E}^i$ is the incident electric field, k_o and η_o are the free space wave number and wave impedance, $\bar{\bar{G}}$ is the dyadic Green's function:

$$\bar{\bar{G}}(\mathbf{r},\mathbf{r}') = j\eta_o k_o \left(\bar{\bar{I}} + \frac{1}{k_o^2} \nabla\nabla \right) g_o(\mathbf{r},\mathbf{r}') \tag{51}$$

$g_o(\mathbf{r},\mathbf{r}') = e^{-jk_o|\mathbf{r}-\mathbf{r}'|} / 4\pi|\mathbf{r}-\mathbf{r}'|$ is the free-space Green's function, and $\mathbf{J}(\mathbf{r})$ is the equivalent current density. Using the method of moment procedure detailed in [2] leads to a discrete linear system of equations:

$$\mathbf{e} = Z\mathbf{b} \tag{52}$$

where Z is a dense matrix, **e** represents the known forcing vector and **b** is the unknown solution vector..

It is assumed that the linear system in (52) will be solved using an iterative scheme. Thus, each iteration will require a matrix vector product. This will be accelerated using the proposed fast scheme. Initially, the impedance matrix is decomposed into two parts:

$$Z = Z^{near} + Z^{far}. \tag{53}$$

where, Z^{near} represent the near-field blocks that are computed to desired precision using adaptive quadrature. Z^{far} represents the far-field blocks that are computed efficiently using single-point evaluations of the kernel. The proposed fast scheme will accelerate the product of the matrix-vector product involving Z^{far}. This is described in the following.

Due to the translational invariance of the Green's function, the convolution of the current with the dyadic Green's function can be computed efficiently for far interactions via the discrete Fourier transform (DFT). Here, the DFT is performed using the "discontinuous-FFT" (D-FFT) recently introduced by Fan and Liu [30]. This method allows one to compute the FFT of a

discontinuous and/or singular function to controllable accuracy. Since the method is based on a quadrature sampling, it is ideal for a Nyström discretization.

Fan and Liu's discontinuous FFT method is extended here to multiple dimensions. Consider the FFT of a multi-dimensional function $f(\mathbf{r})$ distributed on Ω. Ω is discretized into L general curvilinear cells, as governed by the method of moment discretization. The multi-dimensional discrete Fourier transform of $f(\mathbf{r})$ can be defined as:

$$\tilde{f}(\mathbf{n}) = \sum_{l=1}^{L} \int_{\Omega_l} f(\mathbf{r}) e^{j2\pi \mathbf{n}\cdot\mathbf{r}} d\Omega \tag{54}$$

where $\mathbf{n} = (n_1, n_2, \ldots)$ defines the index of the discrete Fourier domain. The integrals are then approximated via an appropriate numerical quadrature rule:

$$\tilde{f}(\mathbf{n}) = \sum_{l=1}^{L} \sum_{q=1}^{N_q} \sqrt{g_q} \omega_q^l f_q^l e^{j2\pi \mathbf{n}\cdot\mathbf{r}_q^l} \tag{55}$$

where $\sqrt{g_q^l}$ is the Jacobian evaluated at the abscissa point $\mathbf{r}_q^l$ on the l-th curvilinear cell, and $f_q^l = f(\mathbf{r}_q^l)$. A uniform grid with spacing $\Delta\mathbf{x}$ is superimposed over the general discretization (see Fig. 7). The indices of the multi-dimensional grid is defined to have physical coordinates $\mathbf{r}_m = (m_1\Delta x, m_2\Delta y, \ldots)$. The exponential function at the indices of the uniform grid is expressed as: $e^{j2\pi \mathbf{n}\cdot\mathbf{r}_m}$. Since the exponential function in (55) is a smooth function over all space, it can be interpolated from the uniform grid indices to the quadrature points as:

$$e^{j2\pi \mathbf{n}\cdot\mathbf{r}_q^l} = \sum_{m=0}^{M} \Phi_m(\mathbf{r}_q^l) e^{j2\pi \mathbf{n}\cdot\mathbf{r}_m} \tag{56}$$

where $\Phi_m(\mathbf{r}_q^l)$ are smooth interpolation polynomials. (It is noted that the summation in (56) is taken over the entire uniform grid. However, the interpolation polynomials $\Phi_m(\mathbf{r}_q^l)$ are non-zero only in a region local to $\mathbf{r}_q^l$). Then, combining (56) with (55), leads to

$$\tilde{f}(\mathbf{n}) = \sum_{l=1}^{L} \sum_{q=1}^{N_q} \sqrt{g_q^l} \omega_q^l f_q^l \sum_{m=0}^{M} \Phi_m(\mathbf{r}_q^l) e^{j2\pi \mathbf{n}\cdot\mathbf{r}_m} \tag{57}$$

The order of summation is then rearranged as:

$$\begin{aligned} \tilde{f}(\mathbf{n}) &= \sum_{m=0}^{M} e^{j2\pi \mathbf{n}\cdot\mathbf{r}_m} \left(\sum_{l=1}^{L} \sum_{q=1}^{N_q} \sqrt{g_q^l} \omega_q^l f_q^l \Phi_m(\mathbf{r}_q^l) f_q^l \right) \\ &= \sum_{m=0}^{M} g_m e^{j2\pi \mathbf{n}\cdot\mathbf{r}_m} \end{aligned} \tag{58}$$

Consequently, $\tilde{f}(\mathbf{n})$ is evaluated efficiently for all values of $\mathbf{n}$ in the discrete space via the FFT.

The discontinuous FFT in (58) is used to evaluate a matrix-vector product involving Z^{far}. Let $\mathbf{j}$ be the vector of currents at the quadrature points. Then, the FFT of $\mathbf{j}$ is expressed in operator format as

$$\tilde{\mathbf{j}}(\mathbf{n}) = \mathcal{F}\{W\mathbf{j}\}. \tag{59}$$

where the operator W is a highly sparse matrix with elements governed by the double summation in (58) and $\mathcal{F}$ is the multi-dimensional FFT. Next, the scattered field due to $\mathbf{j}$ can be computed at the uniform grid points using:

$$\begin{aligned}\mathbf{e}^s(\mathbf{r}_m) &= -\mathcal{F}^{-1}\left\{\mathcal{F}\left\{\bar{\bar{G}}\right\}\cdot\mathcal{F}\left\{V\mathbf{j}\right\}\right\} \\ &= -HW\mathbf{j}\end{aligned}. \tag{60}$$

where the dyadic Green's function $\bar{\bar{G}}$ is evaluated at the uniform grid points referenced to the origin. The field must be evaluated at the quadrature points. Since the field away from the source is smooth, it can be interpolated using the polynomials $\Phi_m\left(\mathbf{r}_q^l\right)$. Consequently,

$$\mathbf{e}^s(\mathbf{r}_q^l) = -V^T HW\mathbf{j}\,. \tag{61}$$

where W is a sparse matrix. Furthermore, it can be shown that $W = \bar{\bar{\omega}}V$, where $\bar{\bar{\omega}}$ is a diagonal matrix with the q_l-th entry $\sqrt{g_q^l\omega_q^l}$.

Finally, we can express:

$$Z^{far}\mathbf{j} = V^T HW\mathbf{j} \tag{62}$$

where $\mathbf{j}$ is the vector of currents at the quadrature points.

Two items should be realized at this point: 1) the far field computation is limited to regions where the fixed point quadrature provides sufficient accuracy to the convolutional operator, and 2) the dyadic Green's function is hypersingular at vanishing separation of the source-observation point pair. Since the FFT is only applied in the far-region, it is sufficient to zero out the dyadic Green's function in the vicinity of the origin. Next, since (62) is a global operator it will lead to non-zero fields in the "near-region". This error is compensated for by "pre-correcting" Z^{near} [10]:

$$\tilde{Z}^{near} = Z^{near} - V^T HW \tag{63}$$

The system matrix in (53) is then expressed as:

$$Z = \tilde{Z}^{near} + V^T HW\,. \tag{64}$$

This fast scheme is referred to here as the QS-PCFFT method. This technique can be compared to both the PC-FFT [10, 31, 32] and AIM methods [11, 33-35]. The most distinctive difference between these techniques and the QS-PCFFT is the projection to the uniform grid. Both the AIM and the P C-FFT methods equate "moments" computed via monomials on the uniform grid and the current basis. This computation is somewhat analogous to computing the weights of a numerical quadrature rule. However, the Gaussian quadrature rule employed by the D-FFT inherently integrates these moments to higher order – even for singular or discontinuous functions using the appropriate quadrature rule. In fact, the weights and abscissa are chosen to realize optimal convergence.

It is next recognized that the QS-PCFFT computes the far interactions to the same precision as the fixed point-quadrature integration. Thus, the precision of the far-field calculation is known

relative to a more rigorous adaptive quadrature evaluation. The break between the near and far interaction is thus specified by the quadrature order and a desired error tolerance.

The complexity and memory requirements of the QS-PCFFT will scale in a similar manner as the PC-FFT and AIM methods. Since Z^{near} is bound near the diagonal, filling and storing this matrix will scale with problem dimension as $O(N)$ (for a fixed order). Furthermore, pre-correcting the near impedance matrix will also scale as $O(N)$ since it is a local operation.

Iterative solutions require a matrix vector multiply, which is performed with the operator in (64). The product with $\tilde{Z}^{near}$ will scale as $O(N)$. The scaling of the product performed via the operator $V^T HW$ will be dependent on the distribution of quadrature points. If the quadrature points densely populate the discrete space so that the uniform FFT grid dimension scales linearly with the number of unknowns, then $V^T HW$ will have a complexity that scales as $O(N \log N)$. However, if the quadrature points sparsely populate the discrete space (e.g., a three-dimensional metallic surface such as a sphere), then the complexity can scale as $O(N^{1/2} \log N)$. Thus, the QS-PCFFT method is most economically applied to problems that involve a more densely distribution of unknowns – that is, where the unknowns occupy much of the problem space.

The QS-PCFFT is an approximation of the convolution rather than an asymptotic expansion of the kernel. Therefore, the dimension of Z^{near} is not a function of electrical lengths, but rather a function of discretization. Consequently, the method can be applied to both low and high frequency problems with equal effectiveness.

To demonstrate the efficiency of the proposed scheme, consider the electromagnetic scattering by an array of circular rings. The unit cell of this array (illustrated in Fig. 8) is situated in a z = constant plane and has a dimension of 1.5 λ x 1.5 λ. The curvilinear cells used to represent the rings are illustrated in Fig. 9. The interpolating grid of a 6th order polynomial cell is also illustrated for one of the cells in ring #2. Jacobi polynomials with singular weights that appropriately model edge singularities were used for basis functions. A Gauss-Jacobi quadrature rule was used for the Nyström formulation and the QS-PCFFT. **Since the quadrature rule integrates the singular basis to high order, the QS-PCFFT is still exponentially convergent – even for singular basis functions.**

The bi-static RCS of a 10 x 10 array of the unit cells is illustrated in Fig. 10 computed with the discretization in Fig. 9, with 3rd order basis and 3 x 3 point quadrature rules on each patch. A 512 x 512 point FFT was used for the QS-PCFFT solution, with the uniform grid being three times the global dimension of the array (45 λ x 45 λ). The error is estimated to be ~1 % for this discretization. The RCS was also computed using FISC [36] employing RWG basis on linear quadrilateral cells [13, 37]. Two different discretizations were used for the FISC simulations resulting in 17,100 (~ 10 cells per wavelength) and 113,400 unknowns (~25 cells per wavelength). The results of the higher discretization is much closer to the LCN solution.

The CPU times and memory of the simulations on a single 750 MHz HP-PARISC processor are recorded in Table 3. (Note that the LCN/QS-PCFFT simulation used double precision, and the FISC simulation used single precision.) It is observed that as the discretization of the FISC simulation was increased, the memory increased more dramatically. The reason for this is that since the finest level of the FMM is fixed. Consequently, the number of cells in the finest groups increases. This increases the dimension of the block matrix that must be stored.

To study the scaling of the complexity of the QS-PCFFT solution, the dimension of the array of circular rings in Fig. 8 was increased from 1×1 to 20×20. The discretization used for each unit cell was fixed to 3rd order basis and 3×3 point Gauss-Jacobi quadrature rules. The size of the FFT was also scaled with the problem domain. The CPU times required for the matrix fill and a matrix-vector multiplication are presented in Fig. 10. Also overlaying these curves are curves illustrating $O(N)$ and $O(N\log N)$ complexity of the tasks, respectively.

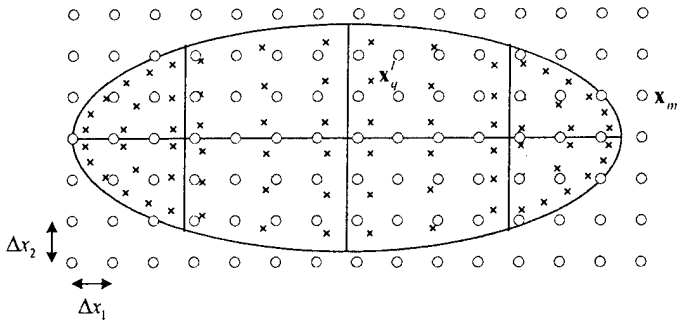

Fig. 20 Uniform grid with spacing $\Delta\mathbf{x}$ indices $\mathbf{x}_m$ overlaying curvilinear cells discretized by quadrature abscissa points $\mathbf{x}_q^l$.

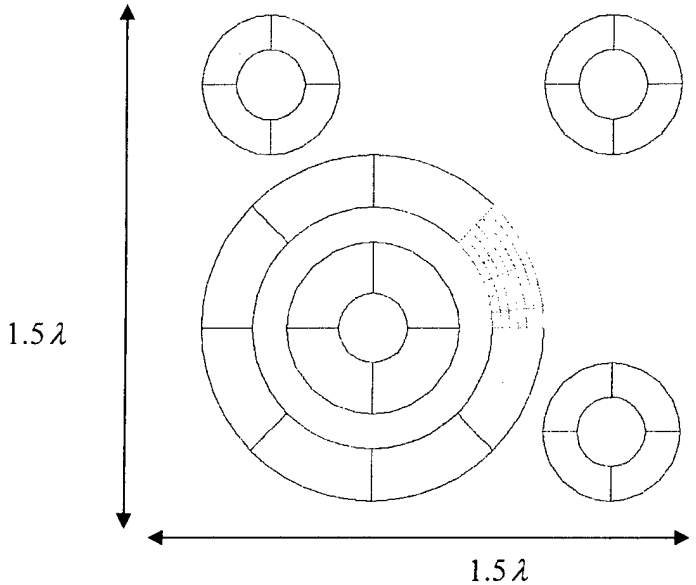

Fig. 21 Illustration of the curvilinear cells used to model one unit cell of the ring array. The center coordinates (x_c, y_c) / Inner/Outer Radius (r_i, r_o) of the five rings are: #1 $(0.5\lambda, 0.5\lambda)/(0.1\lambda, 0.25\lambda)$, #2 $(0.5\lambda, 0.5\lambda)/(0.35\lambda, 0.5\lambda)$, #3 $(0.2\lambda, 1.2\lambda)/(0.1\lambda, 0.2\lambda)$, #4 $(1.2\lambda, 1.2\lambda)/(0.1\lambda, 0.2\lambda)$, #5 $(1.2\lambda, 0.2\lambda)$ $/(0.1\lambda, 0.2\lambda)$ One patch on ring #2 illustrates the discretization of a sixth-order polynomial cell.

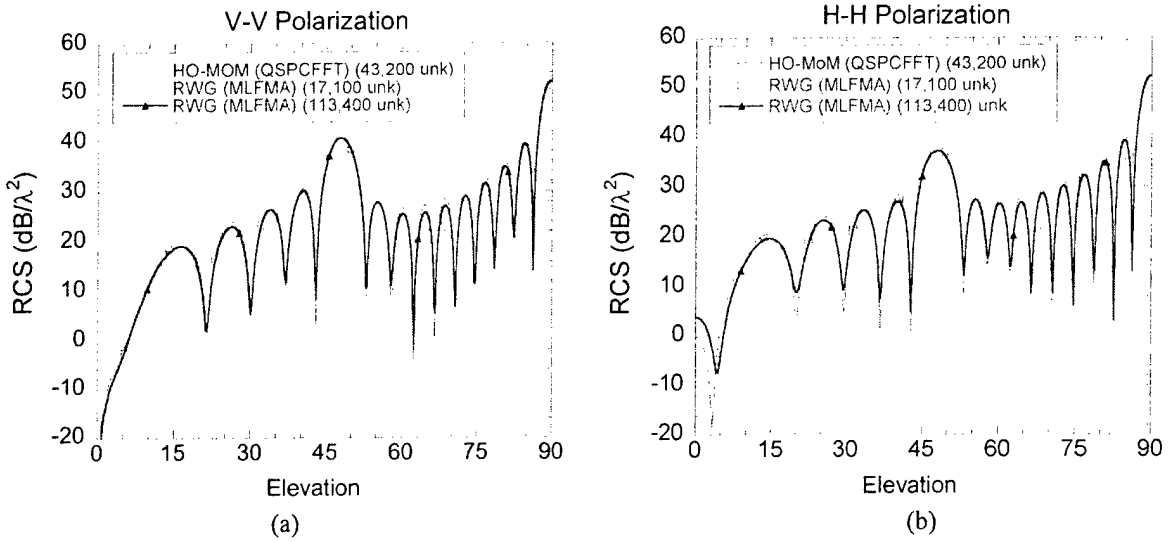

Fig. 22 Bistatic RCS of the ring array with 10×10 unit cells ($a = b = 1.5\ \lambda$) with $(\theta^i, \phi^i) = (0°, 0°)$ computed via the present method as compared and using FISC with RWG basis and the MLFMA [36]. (a) V-V polarization, (b) H-H polarization.

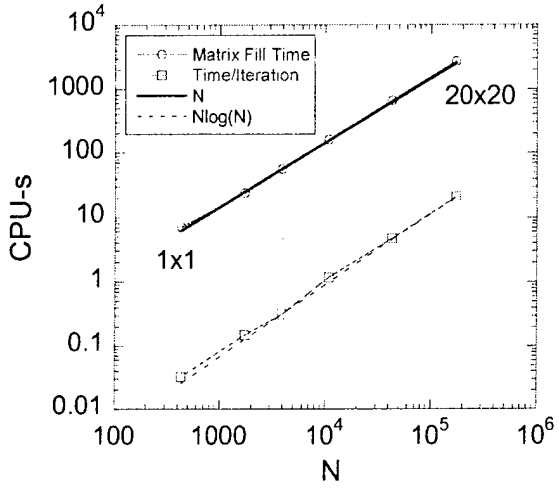

Fig. 23 CPU time for the matrix fill and the time per BICGSTAB iteration versus the number of unknowns recorded on a single 750 MHz HP-PARISC processor as the ring array is scaled from 1×1 to 20×20 array. Also overlaid are curves with slope N and slope of $N\log N$.

	Unknowns	Fill Time	Solve Time	Memory	Total CPU
QSPCFFT	43,200	658 s	415 s	109 MB	1,074 s
FISC	17,100	124 s	1,562 s	32 MB	1,686 s
FISC	113,400	7,930 s	7,930 s	331 MB	11,853 s

Table 3. Scattering by a 10 × 10 circular ring array recorded on a single 750 MHz HP-PARISC processor

4.D.2 The Multilevel Fast Multipole Method (MLFMM)

A fast iterative solver based on the multi-level fast multipole solution [12-15] has also been implemented within *Mat-Scat*. The MLFMM offers a more general fast iterative solution algorithm that will scale as $O(N \log N)$ for general three-dimensional scattering problems. The multi-level scheme implemented is based on the algorithm proposed by Gyuer and Stalzer [16], and the fast spherical filtering scheme of Jakob-Chien and Alpert [17] was implemented to accelerate the disaggregation step of the MLFMM algorithm. For multi-region problems, a separate multipole expansion is performed in each background region.

As an illustration, consider again the EMCC metallic ogive in Fig. 12(a). Both the MLFMM and the QS-PCFFT fast iterative solvers were used to simulate the RCS at 9GHz. The surface was modeled with 288 curvilinear surface cells. The surface currents were modeled with 5^{th} order basis – leading to a total of 11,520 unknowns. For the MLFMM, the smallest group size was set to 0.5 λ_0. The QS-PCFFT used a uniform FFT grid that had a dimension of $108 \times 20 \times 20$. The CPU times and memory required by the fast algorithms are compared with a direct solve in Table 4. A small enough problem was solved to compare against a direct solution algorithm. It is also noted that the results simulated via fast solvers is as accurate as that solved via the direct solver. That is, both the MLFMM and the QS-PCFFT preserves the accuracy of the simulation.

	Filling time (S)	Solving Time (S)	Memory Usage (Mb)
Direct Solver (LU)	1,049	2,239	2025
QS-PCFFT	404	450	46.7
MLFMA	315	540	71.50

CPU time and Memory usage comparison of fast algorithms with direct solver at 9GHz.

4.E High-Order Mesh Generation

High-order methods such as the LCN method are most efficient when employing higher-order basis on large smooth curvilinear patches. The reason for this is simple: higher-order basis converge more rapidly than lower order basis. Thus, with the LCN method it is desirable to model geometries with large curvilinear cells that represent the surface to sufficient accuracy. In practice, cells with average edge lengths on the order of one wavelength are quite typical. Thus, it becomes imperative to employ isoparametric curvilinear patches that accurately model a surface of arbitrary curvature. If one can not support such patches, then one is forced to use a refined discretization – thus losing the advantage of the high-order method. For classical low-order techniques, this has not been an issue since the slow convergence requires one to resolve the surface with a minimum of 10 to 20 edges per linear wavelength to get reasonable accuracy. Often, such fine sampling is also enough to represent a curved surface to sufficient accuracy using a piecewise linear approximation.

Most commercial mesh generation programs are limited by the order of curvilinear cells that can be generated. Most CAD packages provide linear triangles and/or bi-linear quadrilaterals. Some will generate bi-quadratic and very few will generate up to bi-cubic triangle or quadrilateral elements. Unfortunately, this is insufficient for a true high-order method, which requires discretization to arbitrary order. This is illustrated through a simple example. Consider the electromagnetic scattering by a PEC sphere of radius a defined by $k_o a = 6$. The sphere was discretized with 24 quadrilateral curvilinear cells as illustrated in Fig. 24(a). The basis function order was fixed at p = 9, leading to 3,456 unknowns. The bi-static RCS was then predicted by *Mat-Scat* as the order of the curvilinear cell was increased from n = 1 to n = 12. A graph of the error in the RCS relative to an exact Mie-series solution is illustrated in Fig. 24(b). A very important observation is that despite using high-order basis functions (9^{th}-order), the error in the RCS is limited by the error in the discretization of the geometry. That is, if we were limited to bi-cubic quadrilateral cells (3^{rd} order), then the simulation would only provide 2 digits of accuracy despite using 9^{th}-order basis functions. Whereas, minimum error is realized with a mesh that is of order $n = p+1$ (10^{th} order), resulting in 6 digits of accuracy.

The error in the area of the sphere as approximated via a 9×9-point Gauss-Legendre quadrature rule on each patch is also graphed in Fig. 24 (b). It is very interesting to observe that the errors in the RCS and the area follow the same general trend. This shows that there is a direct correlation in the accuracy of the surface model and the accuracy of the EM scattering as predicted by the LCN method. Thus, to accurately and efficiently predict the scattering by com-

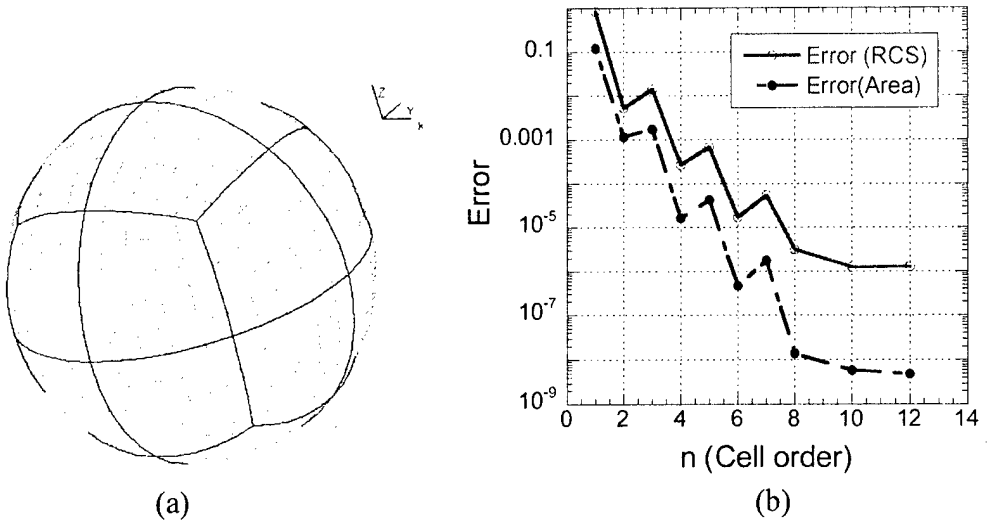

Fig. 24 (a) Illustration of a 24 cell 5th-order quadrilateral discretization of a sphere. (b) Relative mean error in the RCS of a sphere of radius $k_0 a = 6$ computed via the LCN method with ninth-order basis versus the interpolation order n of the 24 curvilinear cells. Also compared in the graph is the relative error of the area of the patched sphere.

plex geometries with a high-order method, it is imperative to have a high-order mesh description.

Currently there are no commercially available CAD tools that provide true high-order modeling. To efficiently model complex geometries with *Mat-Scat*, a high-order mesh description is necessary. Thus, we have developed a mesh processing tool that can generate a high-order mesh, to arbitrary order, from a low-order mesh generated by a commercial CAD tool. The mesh processing tool is named *UKY-MeshTool*. The software has a user friendly GUI interface written in JAVA (see Fig. 25).

The *UKY-MeshTool*, provides high-order surface/volume meshes for:

- Surfaces: high-order quadrilateral or triangular elements.
- Volumes: high-order hexahedral, prism, or tetrahedral elements.

It is emphasized that *MeshTool* does not generate the initial discretization. Rather, it reads in a linear mesh (quadrilateral, triangle, hexahedral, or tetrahedral) generated by another CAD tool Currently, the import format used is the universal file format of SDRC iDEAS™. A high-order mesh is then generated in one of two ways. For canonical geometries, where individual surfaces can be expressed in an analytical form, a scripting software can be used to provide a surface description that *MeshTool* uses to generate a high-order mesh (c.f., Fig. 26). The second manner is to read in a coarse and fine-mesh of the same geometry from the CAD software. This requires the CAD software to support a "mesh-refinement" feature that refines individual elements of a given coarse mesh. *MeshTool* does not require any specification of hierarchy of elements. Rather, it locates nodes shared by the coarse and fine meshes, and then automatically constructs the hierarchy of elements and builds the higher-order mesh.

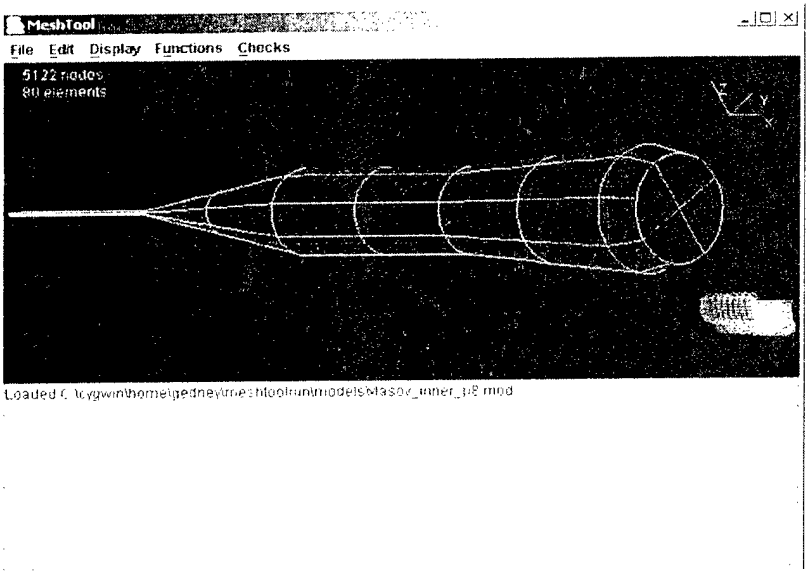

Fig. 25. *UKY-MeshTool* GUI Interface for generating and processing high-order curvilinear meshes.

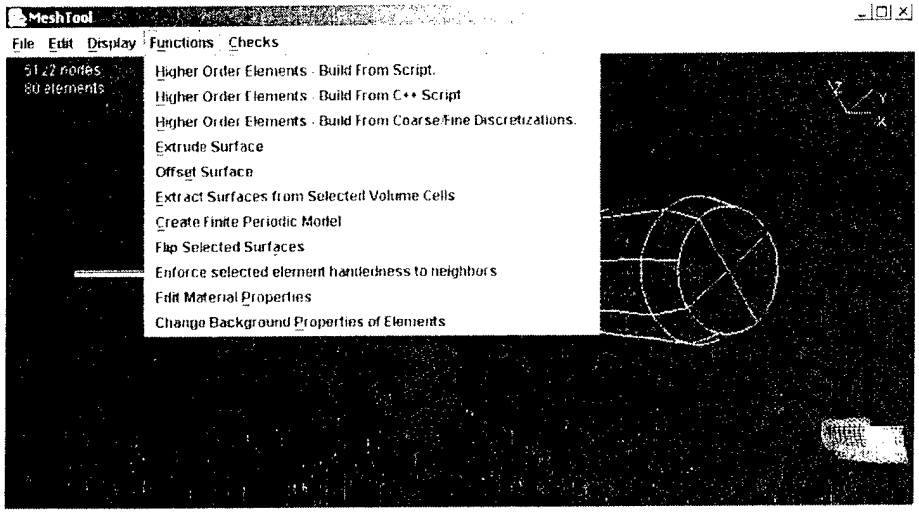

Fig. 26. Functions supported by *UKY-MeshTool*.

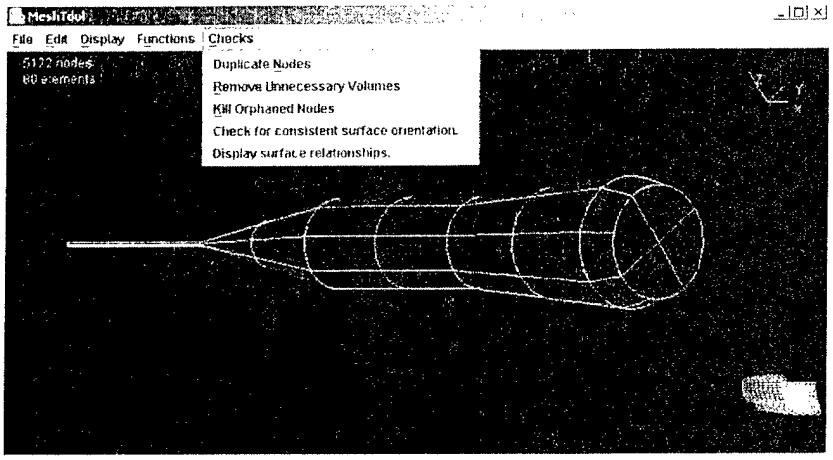

Fig. 27. Mesh checking supported by *UKY-MeshTool*.

Mesh tool also allows the user to extrude volume elements off of a surface. This is useful for creating coatings on a surface, extending a substrate or superstrate, etc. Again, curvilinear offset elements are supported via a scripted description. Alternatively, surface elements can be offset in a similar way for a SIE formulation. Mesh tool will also allow the user to superimpose multiple model geometries. This allows the user to re-use models, or to facilitate the building of more complex structures.

Once a mesh is generated, some mesh quality checking is supported by *MeshTool* such as duplicate node checking (c.f., Fig. 27). It will also compare physical parameters with background parameters and eliminate any volume elements where these are identical since they will support a zero current. Also, when modeling surfaces, the direction of the normal vector as determined by the reciprocal unitary vector $\vec{a}^3$ of the surface patch is important to identify materials above and below. *MeshTool* will check for consistency of surface normal definition, and can flip surface normals locally or globally so that normals are consistent with the surface parameterization.

MeshTool uses standard Legrange interpolation for a geometry description. For example, a quadrilateral patch of order n is represented by $(n+1)\times(n+1)$ nodes that lie on the surface. In the unitary space, these nodes are uniformly spaced, as illustrated in Fig. 28. Each node has a physical coordinate $\vec{r}_{j,k}$ $(j,k=0,n)$. The position at any arbitrary coordinate (u^1,u^2) can be obtained via interpolation:

$$\vec{r}(u^1,u^2)=\sum_{k=0}^{n}\sum_{j=0}^{n}\Phi_j^n\left(u^1\right)\Phi_k^n\left(u^2\right)\vec{r}_{j,k} \tag{65}$$

where the interpolation polynomials are expressed as:

$$\Phi_i^n\left(u\right)=R_i(n,u)R_{n-i}(n,1-u) \tag{66}$$

where $R_i(n,u)$ is a Sylvester interpolation polynomial [38]:

$$R_i(n,u)=\begin{cases}\dfrac{1}{i!}\displaystyle\prod_{k=0}^{i-1}\left(nu-k\right), & 1\le i<n\\ 1, & i=0\end{cases} \tag{67}$$

It is noted that this interpolation procedure exactly represents a bi-linear quadrilateral when $n=1$, bi-quadratic quadrilateral when $n=2$, and a bi-cubic quadrilateral when $n=3$. It also represents interpolations to arbitrary order.

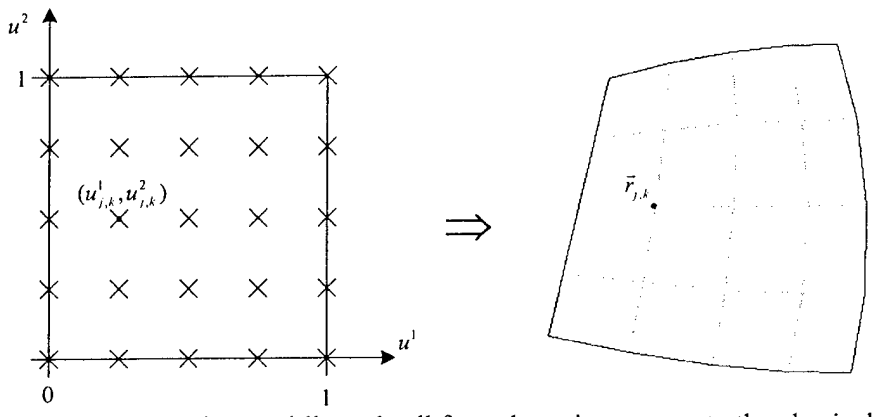

Fig. 28 Mapping of a fourth-order quadrilateral cell from the unitary space to the physical patch.

The unitary vectors for each patch are also readily computed as:

$$\vec{a}_i = \frac{\partial \vec{r}(u^1, u^2)}{\partial u^i} = \frac{\partial}{\partial u^i} \sum_{k=0}^{n} \sum_{j=0}^{n} \Phi_j^n \left(u^1\right) \Phi_k^n \left(u^2\right) \vec{r}_{j,k} \tag{68}$$

Analytical expressions for the derivatives of the interpolation polynomials are easily derived, and the derivatives of the Sylvester interpolation polynomials can be expressed via a recursive relationship that is efficiently computed.

This scheme is general enough to interpolate surfaces up to arbitrary order. However, it still must be realized that the interpolation scheme is only C^0 continuous. And, for very high-orders ($\sim n > 10$) the interpolation operator can be ill conditioned. As a result, Gibb's phenomena can occur leading to small high spatial-frequency oscillation of the interpolated surface. One way that this has been addressed is that *MeshTool* can generate high-order meshes based on a non-uniform Gauss-Lobatto point spacing. Nevertheless, the uniformly spaced interpolation scheme proposed in (65) works quite well to reasonably high order ($\sim 10^{\text{th}}$ order). The non-uniform spaced meshing has shown an improvement in accuracy for higher-order meshes.

Finally, *MeshTool* exports the mesh for *Mat-Scat* and allows the user to define source excitation and post-processing directives (c.f., Fig. 29).

5 Technology Transfer

5.A. Publications

Peer Reviewed Journals

The following papers published in peer reviewed journals have reported in the open literature the results and methodologies developed under this contract:

Dissertations

[1] S. D. Gedney, "High-Order Method of Moment Solution of the Scattering by Three-Dimensional PEC Bodies using Quadrature Based Point Matching," *Microwave and Optical Technology Letters*, vol. 29, pp. 303-309, June 5, 2001. (5)

[2] Stephen D. Gedney, Aiming Zhu , Wee-Hua Tang, Gang Liu, and Peter Petre , "A Fast, High-Order Quadrature Sampled Pre-Corrected FFT for Electromagnetic Scattering," *Microwave and Optical Technology Letters*, vol. 36, no. 5, pp. 343-349, March 5, 2003. (2)

[3] S. D. Gedney and C. C. Lu, "High-Order Solution for the Electromagnetic Scattering by Inhomogeneous Dielectric Bodies," *Radio Science*, vol. 38, no. 1, art. no. 1015, 2003.

[4] G. Liu and S. D. Gedney, "High-Order Moment Method Solution for the Scattering Analysis of Penetrable Bodies," *Electromagnetics*, vol. 23, no. 4, pp. 331-346, 2003.

[5] S. D. Gedney, "On Deriving a Locally Corrected Nyström Scheme from a Quadrature Sampled Moment Method," *IEEE Transactions on Antennas and Propagation*, vol. 51, no. 9, pp. 2402-2412, Sept. 2003.

[6] A. Zhu and S. D. Gedney, "A Quadrature Sampled Pre-Corrected FFT for the Electromagnetic Scattering from Inhomogeneous Objects," *IEEE Antennas and Wireless Propagation Letters*, Vol. 2, no. 1, pp. 50-53, 2003.

[7] S. D. Gedney, A. Zhu, and C. C. Lu, "Study of Mixed-Order Basis Functions for the Locally-Corrected Nyström Method," *IEEE Transactions on Antennas and Propagation*, vol. 52 no. 1, pp. (in press), November 2004.

[8] S. D. Gedney, "Implementing the Locally Corrected Nyström method," *Applied Computational Electromagnetics Society Newsletter*, Vol. 18, no. 3, pp. 15-27, November 2003.

Conference Proceedings – Full Paper

The following papers published as full papers in peer reviewed conference proceedings have reported in the open literature the results and methodologies developed under this contract:

[1] S. Gedney, A. Zhu, W. H. Tang, and P. Petre, "High-Order Pre-Corrected FFT Solution for Electromagnetic Scattering," *2002 IEEE International Symposium on Antennas and Propagation*, San Antonio, TX, June 16-21, 2002.

[2] S. Gedney and C. C. Lu, "High-Order Integral Equation Solution for Scattering by Penetrable Inhomogeneous Volumes," *2002 IEEE International Symposium on Antennas and Propagation*, San Antonio, TX, June 16-21, 2002.

[3] S. Gedney & C. C. Lu, "High-Order Integral Equation Solution Based On a Hybrid Volume/Surface Formulation," *The Annual Review of Progress in Applied Computational Electromagnetics,* Monterey, CA, March 24-28, 2003.

[4] A. Zhu and S. Gedney, " A Fast, High-Order Integral Equation Solution for the Scattering by Inhomogeneous Objects," *2003 IEEE International Symposium on Antennas and Propagation*, Columbus, OH, June 23-27, vol. 1, pp. 7-10, 2003.

[5] S. D. Gedney, R. Hannemann, J. Hannemann, G. Liu, and P. Petre, "A Fast Integral Equation Solution Technique for Printed Circuits in Layered Media," *2003 IEEE International Symposium on Antennas and Propagation*, Columbus, OH, June 23-27, pp. 3 - 6 vol.1, 2003.

[6] S. D. Gedney and C. C. Lu, "High-Order Integral Equation Solution for Scattering by Composite Materials," *2003 IEEE International Symposium on Antennas and Propagation*, Columbus, OH, June 23-27, pp. 1055 - 1058 vol.2, 2003.

[7] S. D. Gedney, A. Zhu, *C.* C. Lu, "High-order Locally Corrected Nystrom Solution with Mixed-order Basis Functions for Electromagnetic Scattering", *ACES Symposium*, Syracuse, NY, April 19-23, paper no. 904178, pg. 1-6, 2004

[8] A. Zhu, S. D. Gedney, "Comparison of Muller and PMCHWT Surface Integral Formulations for the Locally Corrected Nystrom Method", 2004 *IEEE International Symposium on Antennas and Propagation*, Monterey, CA June 21-25, pp. 3871-3874, 2004

[9] A. Zhu, S. D. Gedney, C. Lu, "Fast, High-order, Hybrid Integral Equation Solver for Electromagnetic Scattering," 2004 *IEEE International Symposium on Antennas and Propagation*, Monterey, CA June 21-25, pp. 1199 - 1202, 2004

[10] L. Xuan, A. Zhu, R. J. Adams, S. D. Gedney, "A Broad Band Multilevel Fast Multipole Algorithm", 2004 *IEEE International Symposium on Antennas and Propagation*, Monterey, CA June 21-25, pp. 1195-1198, 2004

[11] S. D. Gedney, A. Zhu, C. C. Lu, "Mixed-Order Basis Functions for the Locally-Corrected Nystrom M ethod," 2004 *I EEE International Symposium on Antennas and Propagation*, Monterey, CA June 21-25, pp. 4044 - 4047, 2004

The following dissertation has resulted from the funding of this program:

Aiming Zhu, Ph.D. Dissertation, *Fast, Hybrid High-Order Integral Solver for Electromagnetic Scattering*, June 2004.

5.B. Inventions

No patents have been applied for from this research.

References

[1] S. D. Gedney, "High-Order Method of Moment Solution of the Scattering by Three-Dimensional PEC Bodies using Quadrature Based Point Matching," *Microwave and Optical Technology Letters*, vol. 29, no. 5, pp. 303-309, June 5 2001.

[2] S. D. Gedney, "On Deriving a Locally Corrected Nyström Scheme from a Quadrature Sampled Moment Method," *IEEE Transactions on Antennas and Propagation*, vol. 51, no. 9, pp. 2402-2412, September 2003.

[3] L. F. Canino, J. J. Ottusch, M. A. Stalzer, J. L. Visher, and S. M. Wandzura, "Numerical solution of the Helmholtz equation in 2D and 3D using a high-order Nyström discretization," *Journal of Computational Physics*, vol. 146, no. 2, pp. 627-663, 1998.

[4] S. D. Gedney, A. Zhu, W.-H. Tang, G. Liu, and P. Petre, "A Fast, High-Order Quadrature Sampled Pre-Corrected FFT for Electromagnetic Scattering," *Microwave and Optical Technology Letters*, vol. 36, no. 5, pp. 343-349, March 5 2003.

[5] S. Gedney, A. Zhu, and C. C. Lu, "Study of Mixed-Order Basis Functions for the Locally-Corrected Nyström Method," *IEEE Transactions on Antennas and Propagation*, vol. 52, no. 11, in press, November 2004.

[6] G. Liu and S. D. Gedney, "High-order Nyström solution of the volume EFIE for TM-wave scattering," *Microwave and Optical Technology Letters*, vol. 25, no. 1, pp. 8-11, 2000.

[7] G. Liu and S. D. Gedney, "High-Order Nyström Solution of the Volume EFIE for TE-Wave Scattering," *Electromagnetics*, vol. 21, no. January-February, pp. 1-14, 2001.

[8] S. D. Gedney and C. C. Lu, "High-Order Solution for the Electromagnetic Scattering by Inhomogeneous Dielectric Bodies," *Radio Science*, vol. 38, no. 1, pp. 1015, February 2003.

[9] A. Zhu and S. D. Gedney, "A Quadrature Sampled Pre-Corrected FFT Method for the Electromagnetic Scattering from Inhomogeneous Objects," *IEEE Antennas and Wireless Propagation Letters*, vol. 2, no. 1, pp. 50-53, 2003.

[10] J. R. Phillips and J. K. White, "A precorrected-FFT method for electrostatic analysis of complicated 3-D structures," *IEEE Transactions on Computer-Aided Design of Integrated Circuits and Systems*, vol. 16, no. 10, pp. 1059-1072, 1997.

[11] E. Bleszynski, M. Bleszynski, and T. Jaroszewicz, "AIM: Adaptive Integral Method for Solving Large-Scale Electromagnetic Scattering and Radiation Problems," *Radio Science*, vol. 31, no. 5, pp. 1225-1251, 1996.

[12] R. Coifman, V. Rokhlin, and S. M. Wandzura, "The fast multipole method for the wave equation: A pedestrian prescription," *IEEE Antennas and Propagation Society Magazine*, vol. 35, no. June, pp. 7-12, 1993.

[13] J. M. Song and W. C. Chew, "Fast Multipole Method Solution Using Parametric Geometry," *Microwave and Optical Technology Letters*, vol. 7, no. 16, pp. 760-765, Nov 1994.

[14] J. M. Song and W. C. Chew, "Multilevel Fast-Multipole Algorithm for Solving Combined Field Integral-Equations of Electromagnetic Scattering," *Microwave and Optical Technology Letters*, vol. 10, no. 1, pp. 14-19, 1995.

[15] J. M. Song, C. C. Lu, and W. C. Chew, "Multilevel fast multipole algorithm for electromagnetic scattering by large complex objects," *IEEE Transactions on Antennas and Propagation*, vol. 45, no. 10, pp. 1488-1493, 1997.

[16] M. F. Gyure and M. A. Stalzer, "A prescription for the multilevel Helmholtz FMM," *IEEE Computational Science & Engineering*, vol. 5, no. 3, pp. 39 -47, July-September 1998.

[17] R. JakobChien and B. K. Alpert, "A fast spherical filter with uniform resolution," *Journal of Computational Physics*, vol. 136, no. 2, pp. 580-584, Sep 15 1997.

[18] J. A. Stratton, *Electromagnetic Theory*. New York: McGraw-Hill, 1941.

[19] F. Çaliskan and A. F. Peterson, "The need for mixed-order representations with the locally corrected Nystrom method," *IEEE Antennas and Wireless Propagation Letters*, vol. 2, no. 1, pp. 72- 73, 2003.

[20] D. E. Livesay and K. M. Chen, "Electromagnetic fields induced inside arbitrarily shaped biological bodies," *IEEE Transactions on Microwave Theory and Techniques*, vol. MTT-22, pp. 1273-1280, December 1974.

[21] D. H. Schaubert, D. R. Wilton, and A. W. Glisson, "A Tetrahedral Modeling Method for Electromagnetic Scattering by Arbitrarily Shaped Inhomogeneous Dielectric Bodies," *IEEE Transactions on Antennas and Propagation*, vol. 32, no. 1, pp. 77-85, 1984.

[22] A. F. Peterson, S. L. Ray, and R. Mittra, *Computational Methods for Electromagnetics*. New York: IEEE Press, 1998.

[23] J. R. Mautz and R. F. Harrington, "Electromagnetic scattering from a homogeneous material body of revolution," *AEU*, vol. 33, pp. 71-80, February 1979.

[24] A. A. Kishk and L. Shafai, "Different Formulations for Numerical Solution of Single or Multibodies of Revolution with Mixed Boundary Conditions," *IEEE Transactions on Antennas and Propagation*, vol. AP-34, no. 5, pp. 666-673, May 1986.

[25] C. Müller, *Foundations of the Mathematical Theory of Electromagnetic Waves*, vol. 301. Berlin: Springer-Verlag, 1969.

[26] A. C. Woo, H. T. G. Wang, M. J. Schuh, and M. L. Sanders, "Benchmark plate radar targets for the validation of computational electromagnetic programs," *IEEE Antennas and Propagation Magazine*, vol. 36, no. 6, pp. 52-56, December 1992.

[27] A. C. Woo, H. T. G. Wang, and M. J. Schuh, "Benchmark radar targets for the validation of computational electromagnetics programs," *IEEE Antennas and Propagation Magazine*, vol. 35, no. 1, pp. 84-89, February 1993.

[28] W. C. Chew, J. M. Jin, C. C. Lu, E. Michielssen, and J. M. M. Song, "Fast solution methods in electromagnetics," *IEEE Transactions on Antennas and Propagation*, vol. 45, no. 3, pp. 533-543, 1997.

[29] K. C. Donepudi, J. M. Jin, and W. C. Chew, "A higher-order multilevel fast multipole algorithm for scattering from mixed conducting/dielectric bodies," *IEEE Transactions on Antennas and Propagation*, vol. 51, no. 10, pp. 2814-2821, October 2003.

[30] G. X. Fan and Q. H. Liu, "The CGFFT method with a discontinuous FFT algorithm," *Microwave and Optical Technology Letters*, vol. 29, no. 1, pp. 47-49, 2001.

[31] X. Nie, L. W. Li, N. Yuan, and J. K. White, "Fast analysis of scattering by arbitrarily shaped three-dimensional objects using the precorrected FFT method," *IEEE Transactions on Antennas and Propagation*, vol. to appear, no., 2003.

[32] N. Yuan, T. S. Yeo, X. Nie, and L. W. Li, "A fast analysis of scattering and radiation of large microstrip antenna arrays," *IEEE Transactions on Antennas and Propagation*, vol. 51, no. 9, pp. 2218 - 2226, September 2003.

[33] F. Ling, C. F. Wang, and J. M. Jin, "Application of adaptive integral method to scattering and radiation analysis of arbitrarily shaped planar structures," *Journal of Electromagnetic Waves and Applications*, vol. 12, no. 8, pp. 1021-1037, 1998.

[34] C. F. Wang, F. Ling, J. M. Song, and J. M. Jin, "Adaptive integral solution of combined field integral equation," *Microwave and Optical Technology Letters*, vol. 19, no. 5, pp. 321-328, Dec 5 1998.

[35] S. S. Bindiganavale, J. L. Volakis, and H. Anastassiu, "Scattering from planar structures containing small features using the adaptive integral method (AIM)," *IEEE Transactions on Antennas and Propagation*, vol. 46, no. 12, pp. 1867-1878, Dec 1998.

[36] J. M. Song, C. C. Lu, W. C. Chew, and S. W. Lee, "Fast Illinois Solver Code (FISC)," *IEEE Antennas and Propagation Magazine*, vol. 40, no. 3, pp. 27-34, Jun 1998.

[37] J. M. Song and W. C. Chew, "Moment Method Solutions Using Parametric Geometry," *Journal of Electromagnetic Waves and Applications*, vol. 9, no. 1-2, pp. 71-83, 1995.

[38] P. P. Silvester and R. L. Ferrari, *Finite Elements for Electrical Engineers*, 2nd ed. Cambridge: Cambridge University Press, 1990.